Activated interstitial macrophages are a predominant target of viral takeover and focus of inflammation in COVID-19 initiation in human lung

Timothy Ting-Hsuan Wu[1,9,*], Kyle J. Travaglini[1,9,†,*], Arjun Rustagi[2,7,*,**], Duo Xu[1,13], Yue Zhang[1,9,11], SoRi K. Jang[1,9], Astrid Gillich[1,9,†], Roozbeh Dehghannasiri[1,6], Giovanny Martinez-Colon[2,7], Aimee Beck[2], Aaron J. Wilk[2,7], Maurizio Morri[10], Winston L. Trope[3], Joseph B. Shrager[3,8], Stephen R. Quake[10,12], Christin S. Kuo[5], Julia Salzman[1,6], Peter S. Kim[1,10,13], Catherine A. Blish[2,7,10,**], and Mark A. Krasnow[1,4,9,**]

[1]Department of Biochemistry,
[2]Department of Medicine, Division of Infectious Diseases,
[3]Department of Cardiothoracic Surgery,
[4]Vera Moulton Wall Center for Pulmonary Vascular Disease,
[5]Department of Pediatrics, Pulmonary Medicine,
[6]Department of Biomedical Data Science,
[7]Program in Immunology,
Stanford University School of Medicine, Stanford, CA, USA 94305.

[8]Veterans Affairs Palo Alto Healthcare System, Palo Alto, CA, USA

[9]Howard Hughes Medical Institute.

[10]Chan Zuckerberg Biohub, San Francisco, CA, USA.

[11]Department of Biology,
[12]Department of Bioengineering,
[13]Stanford ChEM-H,
Stanford University, Stanford, CA, USA 94305.

* These authors contributed equally to this work
** Corresponding authors. A. R. (arjun.rustagi@stanford.edu), C. A. B. (cblish@stanford.edu), and M.A.K. (krasnow@stanford.edu).

† Present address: Allen Institute for Brain Science, Seattle, WA, USA (K.J.T) Calico Life Sciences, South San Francisco, CA USA (A.G)

ABSTRACT

Early stages of deadly respiratory diseases such as COVID-19 have been challenging to elucidate due to lack of an experimental system that recapitulates the cellular and structural complexity of the human lung, while allowing precise control over disease initiation and systematic interrogation of molecular events at cellular resolution. Here we show healthy human lung slices cultured *ex vivo* can be productively infected with SARS-CoV-2, and the cellular tropism of the virus and its distinct and dynamic effects on host cell gene expression can be determined by single cell RNA sequencing and reconstruction of "infection pseudotime" for individual lung cell types. This revealed the prominent SARS-CoV-2 target is a population of activated interstitial macrophages, which as infection proceeds accumulate thousands of viral RNA molecules per cell, comprising up to 60% of the cellular transcriptome and including canonical and novel subgenomic RNAs. During viral takeover, there is cell-autonomous induction of a specific host interferon program and seven chemokines (*CCL2*, 7, *8*, *13, CXCL10*) and cytokines (*IL6, IL10)*, distinct from the response of alveolar macrophages in which neither viral takeover nor induction of a substantial inflammatory response occurs. Using a recombinant SARS-CoV-2 Spike-pseudotyped lentivirus, we show that entry into purified human lung macrophages depends on Spike but is not blocked by cytochalasin D or by an ACE2-competing monoclonal antibody, indicating a phagocytosis- and ACE2-independent route of entry. These results provide a molecular characterization of the initiation of COVID-19 in human lung tissue, identify activated interstitial macrophages as a prominent site of viral takeover and focus of inflammation, and suggest targeting of these macrophages and their signals as a new therapeutic modality for COVID-19 pneumonia and progression to ARDS. Our approach can be generalized to define the initiation program and evaluate therapeutics for any human lung infection at cellular resolution.

INTRODUCTION

Lower respiratory infections are one of the leading causes of death worldwide[1,2], accelerated by the current Coronavirus Disease 2019 (COVID-19) pandemic[3]. Most such infections, including COVID-19, start innocuously in the upper respiratory tract and become dangerous when they reach alveoli[4-9], the site of gas exchange, but the critical transition to life threatening pneumonia and acute respiratory distress syndrome (ARDS) has been difficult to elucidate. For practical and ethical reasons, such early and key steps in human pathogenesis have been inferred, with rare exception[10,11], from examination of late or end stage patient lung lavage, biopsy, or autopsy specimens, using classical histopathological methods[12-14] and recently single cell multi-omic profiling[15-20].

These approaches provide a picture of COVID-19 pneumonia at unprecedented cellular and molecular resolution, and have suggested models of pathogenesis involving not only infection of the alveolar epithelium but also implicating alveolar capillaries, macrophages and other myeloid cells[18,19,21-23] and production of various inflammatory cytokines and chemokines[15,19]. It remains unclear which cells are the direct virus targets in the human lung, and the nature of their virus-induced host response – in particular, the origin and sequence of molecular signals that initiate, sustain, and propagate the inflammatory cascade that leads to COVID-19 ARDS[4].

These early pathogenic events hold the key to understanding and preventing the transitions to the deadly and systemic forms of COVID-19, but we know little about them. This is due to difficulty accessing human lung tissue at this critical transition, and the sheer number of lung (>58) and alveolar (14) cell types potentially involved. This cellular complexity has made

pathogenic mechanisms challenging to empirically address even in the most sophisticated human lung organoid systems[24-27] and animal models[5-7,20,28-31].

Here we describe an experimental model of SARS-CoV-2 infection that allows systematic interrogation of the early molecular events and pathogenic mechanism of COVID-19 at cellular resolution in native human lung tissue. We determine the cellular tropism of SARS-CoV-2 and its distinct and dynamic effects on host cell gene expression for individual lung cell types. The most prominent target is a population of interstitial macrophages in which the virus takes over the transcriptome and induces a specific host interferon program along with seven chemokines and cytokines that can signal to a diverse array of lung immune and structural cell types that express the cognate receptors. We propose that this early focus of lung inflammation is a key step in the transition to the deadly and systemic forms of COVID-19 and a potential new therapeutic target.

RESULTS

Human lung slices cultured *ex vivo* are productively infected by SARS-CoV-2

To define the early events of SARS-CoV-2 infection in human lung, we cut thick sections (~300-500 μm "slices") of fresh lung tissue procured from therapeutic surgical resections or organ donors, and placed the slices in culture medium containing DMEM/F12 and 10% FBS (Fig. 1a). We then infected them with SARS-CoV-2 (USA-WA1/2020) at a multiplicity of infection (MOI) of 1 for two hours, and the cultures continued for 24 or 72 hours to allow infection to proceed. Plaque assay of culture supernatants demonstrated production of infectious virions that increased between 24 and 72 hours of culturing (Fig. 1b, Extended Data Fig.1). Productive infection was abrogated by pre-inactivation of the viral stocks with heat or ultraviolet

light, or by addition to the slice culture medium of 10 μM remdesivir, an RNA-dependent RNA polymerase inhibitor used as a COVID-19 therapeutic (Fig. 1b).

To characterize viral and host gene expression during SARS-CoV-2 infection, slices were dissociated and analyzed by single-cell RNA sequencing (scRNA-seq, 10x Genomics), adapting the methods we and others previously used to construct a comprehensive transcriptomic atlas of the healthy human lung[32-38] to capture, quantify, and map SARS-CoV-2 viral gene expression along with host gene expression in each profiled lung cell[39,40]. The number of viral RNA molecules detected per infected cell spanned a wide range (Fig.1c, d), with the vast majority (~99%) of profiled cells from infected lung slices containing few or no detected viral RNA molecules (Fig. 1d). But the rest of the cells (~1%) expressed tens to hundreds of viral RNA molecules per cell at 24 hours, and by 72 hours the distribution had shifted to even higher values with rare cells (~0.01%) accumulating thousands of viral RNAs per cell (Fig. 1d), paralleling the increase in virus production during this period (Extended Data Fig.1). As with infectious virions, viral RNA levels determined by scRNA-seq were diminished by inactivation of the virus stocks with heat or ultraviolet irradiation, or by addition to the culture medium of remdesivir (Fig. 1c).

We also investigated the junctional structure and processing of the viral RNA molecules by analyzing our scRNA-seq dataset using the SICILIAN framework[41], which identifies RNA sequencing reads that map discontinuously in a genome, such as reads that span splice junctions of eucaryotic mRNAs or the subgenomic junctions of the nested SARS-CoV-2 mRNAs. We detected canonical subgenomic junctions among the rare sequence reads outside their 3' ends, confirming generation of canonical SARS-CoV-2 mRNAs in the lung slice cultures (Fig. 1c, right panel). In addition, we identified dozens of novel subgenomic junctions, indicating widespread generation of diverse non-canonical subgenomic viral RNAs along with canonical

subgenomic forms during lung infection (Fig. 1c, Extended Data Fig. 2, Table S1). These non-canonical junctions included three that spliced the standard viral 5' leader sequence to a novel downstream site, as well 494 junctions between two novel internal sites in the genome and 479 junctions between an internal and 3' site (the most abundant non-canonical species detected, consistent with the strong 3' end bias of 10x technology). Some of these non-canonical RNAs are predicted to encode novel viral proteins, or alter potential regulatory sequences in the 3' non-coding region of the viral mRNA. Heat inactivation or ultraviolet irradiation of the viral stocks, or remdesivir addition, abrogated formation of both canonical and non-canonical junctions (Fig. 1c, right panel). Together, these data demonstrate that lung cultures support ongoing, productive viral replication.

A cellular atlas of SARS-CoV-2 tropism in the human lung

The cellular tropism of a virus – the set of host cells that allow viral entry and replication – is among the most characteristic and significant determinants of virulence. Historically tropism has been inferred from autopsy specimens, often weeks, months, or even years after disease onset. More recently, tropism has been predicted from expression patterns of entry receptors identified by biochemical or functional screening in heterologous cell types[42]. For SARS-CoV-2, a small subset of lung epithelial types (AT2, ciliated, AT1, club, and goblet cells) were predicted to be the major direct targets for SARS-CoV-2 based on their expression of the canonical SARS-CoV-2 receptor ACE2 and protease TMPRSS2[18,24,32,43]. However, studies of COVID-19 autopsy lungs have detected viral gene products in various epithelial and endothelial cells, fibroblasts, and myeloid cells, indicating widespread viral presence at least in end-stage disease[18,19].

To determine SARS-CoV-2 lung cell tropism empirically and directly compare infection of lung cell types in their natural context, we first used the most sensitive and specific markers

from our molecular atlas of the healthy human lung[32] to identify the cell types present in the cultured lung slices from their transcriptomic profiles, and then assessed their viral RNA levels in the infected cultures. Of the 176,382 cells with high quality transcriptomes obtained from infected lung slices of four donor lungs, along with those of the 112,359 cells from mock-infected slices (cultured without viral addition) and 95,389 uncultured control cells (from freshly-cut lung slices), we identified 55 distinct molecular lung cell types distributed across the major tissue compartments (Fig. 2a, Extended Data Fig. 3, Table S2). These included most (46 out of 58, 80%) of the cell types described in the healthy human lung[32] plus 5 additional types of lymphocytes (e.g., CD4+ cytotoxic T lymphocytes, γδ T cells, regulatory T cells, tissue-resident memory CD8+ T cells, GZMK+CD8+ T cell; Fig. 2a, blue) along with culture-induced proliferative states of signaling alveolar type 2 (AT2-s) cells, NK cells, and dendritic cells (DCs) and several culture-induced proliferative and activation states of fibroblasts, which could not be ascribed to any previously defined fibroblast types (Fig. 2a, grey). The only cell types not recovered after culturing were rare myeloid types (e.g., IGSF21+ DCs, TREM2+ DCs, classical monocytes), which may egress from the slices or not survive during culture (Extended Data Fig.3, Table S2).

Cellular SARS-CoV-2 viral RNA levels across the 55 human lung cell types in the infected cultures are shown in Fig. 2a. Although 10-20 viral RNA molecules were detected in about one-third of the molecular cell types in the infected cultures, cells with high viral levels (hundreds to thousands of SARS-CoV-2 UMI per cell) were rare and restricted to six cell types. One was AT2 cells, a predicted target of SARS-CoV-2. The others had not been previously shown to directly support viral replication or production, and included myofibroblasts, lipofibroblasts, two molecular types of T cells and NK cells, and macrophages. Macrophages

were the most prominent lung targets, accounting for 75% of cells with 50 or more viral UMI per cell. However, even for macrophages, such cells represented only a small proportion of the recovered cell type (0.5% of all macrophages), indicating inefficient access or entry or a sensitive subpopulation (see below). One caveat to this tropism analysis is that identities could not be assigned to 16% of cells with 50 or more viral UMI per cell because they did not robustly express cell type markers ("unidentified" cell types, Fig. 2a), presumably due to downregulation of the host transcriptome during viral takeover. Most cells with high viral load were detected in cultures at 72 but not 24 hours after infection, indicating that the intervening 48 hours is the critical period of viral RNA amplification in most lung cell types.

To validate these lung cell tropism results, visualize the infected cells, and localize foci of viral replication, we performed multiplexed single molecule fluorescence *in situ* hybridization (smFISH) of the infected lung slices to simultaneously detect positive strand viral RNA (S gene probe), negative strand viral RNA (replication intermediate, Orf1ab gene probe), the canonical viral receptor ACE2, and markers of the infected cell types detected in scRNA-seq (Fig. 2b,c). We found both positive and negative strand viral RNA in AT2 cells (*SFTPC*$^+$*EPCAM*$^+$), myofibroblasts (*ASPN*$^+$*COL1A2*$^+$), macrophages (*PTPRC*$^+$*MARCO*$^+$) and exceedingly rarely, CD4 T cells (*PTPRC*$^+$*CD3*$^+$*CD4*$^+$). We also detected cells filled with viral mRNA molecules but no negative strand RNA, the early replication intermediate, or any of the cell-type markers in our panel; these are likely cells at an advanced stage of viral takeover, nearing cell lysis. Infected cells were generally scattered throughout the infected lung tissue, but rare clusters were detected such as an infected macrophage associated with two CD4 T cells (Fig. 2d).

For AT2 cells, myofibroblasts, and T cells, the cells with high viral load were rare in the tissue sections, as in the scRNA-seq tropism analysis. In contrast, infected macrophages were

more abundant and showed a broad and seemingly continuous range of viral RNA molecules. Some macrophages (*PTPRC*$^{+}$*MARCO*$^{+}$) showed a few (1-3 puncta) positive-strand viral RNA molecules but no negative strand viral RNA, whereas others expressed a few (1-3 puncta) negative strand viral RNA molecules alongside a wide range (1 to dozens of puncta) of positive strand viral RNA molecules (Fig. 2c).

SARS-CoV-2 takeover of an activated interstitial macrophage subtype

We reasoned that the macrophages in the lung slice cultures with SARS-CoV-2 RNA levels spanning several orders of magnitude – from tens to thousands of UMIs in the scRNA-seq analysis (Fig. 2a) and from one to dozens of puncta detected by smFISH (Fig. 2c) – were infected cells harboring active intermediates that had progressed to different stages of infection, those with highest RNA loads having progressed furthest in the infection cycle. This is consistent with our finding that cells harvested 72 hours after infection generally had higher viral RNA levels than those harvested at 24 hours (Fig. 1d).

To resolve the apparent heterogeneity in the infected macrophages, we further clustered the gene expression profiles of macrophages in the lung slices and found that they separated into three distinct clusters (Fig. 3a). One had higher expression of genes involved in functions ascribed to mature alveolar macrophages, including antigen-presentation major histocompatibility complex class II (MHCII) genes (*HLA-DPA1*, *HLA-DPB1*, *HLA-DQA1*, *HLA-DQB1*, and *CD74*) and genes involved in lipid homeostasis (*LPL*, *APOC1*, *FABP3*, *FABP4*, and *HPGD*; Fig. 3c,d)[44]. smFISH showed cells expressing these markers were larger and rounder in morphology than the others, and localized to the alveolar airspace (Fig. 3b,e,f), hence we refer to them as “alveolar macrophages” (AMs). Another cluster we call “interstitial macrophages” (IMs) expressed lower levels of the classical AM markers including *LPL*, *APOC1*, *FABP3*, *FABP4*,

and *HPGD* but were enriched for a different set of genes including the monocyte marker CD14 (Fig. 3c,d), and localized interstitially (Fig. 3b,e,f, Extended Data Fig. 4). The third cluster was transcriptionally similar to interstitial macrophages but also expressed genes known to be activated by NF-KB signaling (*NFKBIA*, *NFKBIZ*, and *IL1B*), inflammation (*IER3*, *EREG*, *TIMP1*, *STAB1*), and hypoxia-induced factor *HIF1A*; we call them "activated interstitial macrophages" (Fig. 3c,d, a-IMs). Although a-IMs were detected in the uncultured control lung slices, they were a minor population. However, upon culturing, almost all IMs became activated; indeed, this was among the most robust transcriptional changes we observed in the control (mock-infected) lung slice cultures. Similar populations of activated lung macrophages have been observed infiltrating tumors in the intact human lung[45,46] and in other inflammatory conditions[47,48].

Comparison of SARS-CoV-2 infection of the macrophage subtypes in the slice cultures revealed a striking difference in viral RNA accumulation in AMs vs. a-IMs. Although both AMs and a-IMs could accumulate hundreds of viral RNAs, only in a-IMs did viral RNA accumulate beyond 300 viral UMI per cell and result in viral domination ("takeover") of the host cell transcriptome (Fig. 3g). Viral takeover reached up to 60% of an a-IM transcriptome (ratio of viral to total UMIs in a cell), whereas it never exceeded 2% of an AM transcriptome (Fig. 3g). Thus, in a-IMs, SARS-CoV-2 can infect and amplify its RNA until it dominates the host transcriptome, whereas viral RNA takeover does not occur in AMs.

Infection pseudotime of activated interstitial macrophages reveals an early focus of lung inflammation

To characterize the host cell response during viral takeover, we computationally ordered the infected macrophages according to the principal components that best correlated with viral

RNA levels and takeover to reconstruct what we refer to as "infection pseudotime" (Fig. 4a, Extended Data Fig. 5), similar to developmental pseudotime[49,50], providing a dynamic view of the viral gene expression program and its effect on the host transcriptome.

Differential gene expression analysis[51] of a-IMs along infection pseudotime identified host gene expression changes that correlated with viral RNA levels (Table S3); the kinetics of induction of individual genes in infection pseudotime is shown in Fig. 4b-f. A specific set of antiviral genes was upregulated during viral amplification, including the earliest, interferon regulatory factor 3 (IRF3)-dependent type I interferon response genes (*ISG15*, *ISG20*, *IFIT1*, *IFITM3*, *OAS1*, *RSAD2*, *MX1*, *MX2*; Fig. 4b)[52-55] and many additional canonical interferon-stimulated genes (ISGs; *IFI44*, *IFI44L*, *IFIH1*, *LPAR6*, *USP18*, *HELZ2*, *IFITM1*, *IFITM2*, *STAT1*, *DDX58*, *OAS3*, *XAF1*; Fig. 4c)[56]. This appears to be the cell intrinsic response to infection, presumably resulting from detection of accumulating viral RNA. Viral amplification in a-IMs was also associated with induction of five chemokines (*CCL2*, *CCL7*, *CCL8*, *CCL13*, *CXCL10*; Fig. 4d)) and two cytokines (*IL6*, *IL10*; Fig. 4e), including the pro-inflammatory cytokine IL6 central to COVID-19 cytokine storm[57]. In contrast, viral RNA amplification was associated with reduced expression of chemokines *CXCL1*,*2,3,5*, and *8* (Table S3).

Alveolar macrophages showed a distinct and more limited response to the virus (Table S3, Fig. 4f). During infection pseudotime, only a handful of genes were specifically induced, including *APOC1*, *FDX1*, *IFI27*, *HLA-DRB1*, serine proteases *SERPINA1* and *SERPING1,* and *CXCL16*. Expression of nearly all other chemokines (*CXCL1*, *CXCL2*, *CXCL3*, *CXCL5*, *CXCL8*, *CCL3*, *CCL4*, *CCL20*) was downregulated in AMs.

To predict the cellular targets of the inflammatory signals induced by SARS-CoV-2 infection of a-IMs, we used the single cell gene expression profiles of the infected lung slices to

produce a map of cells expressing the cognate receptors (Fig. 4g). Viral induction of *CXCL10* in a-IMs predicts communication to and recruitment of broad classes of CD4 and CD8 T cells via the cognate receptor *CXCR3*, consistent with our observation by smFISH that T cells interacted directly with infected a-IMs. (Fig. 2d). Viral induction of *CCL2* predicts recruitment of specific DC subtypes (maDCs, mDC2) through *CCR2*, and induction of *CCL8* could recruit neutrophils and create a self-amplifying circuit with macrophages via *CCR1* (Fig. 4h). The specific viral induction of *IL6* and *IL10* along infection pseudotime that can signal through its cognate receptors to most other structural (*IL6*) and immune (*IL6, IL10*) cell types of the lung indicates that infected a-IMs could broadcast inflammatory signals widely in the lung (Fig. 4h).

We conclude that infection and takeover of a-IMs induces a robust cell intrinsic response to the virus and creates an immune signaling center and focus of inflammation in early SARS-CoV-2 infection, whereas infected AMs restrict viral RNA amplification and generally suppress their communication to other immune cell types.

Lung macrophage entry is not neutralized by ACE2-competing antibodies

Activated interstitial macrophages did not express detectable levels of *ACE2*, the canonical SARS-CoV-2 receptor, by scRNA-seq (Extended Data Fig. 6) or by smFISH (Fig. 2c). To explore the mechanism of SARS-CoV-2 entry into human lung macrophages, we modified a recombinant Spike-pseudotyped lentivirus system[58] to carry a nanoluciferase (NLuc) bioluminescence and tdTomato fluorescence dual readout (lenti-S-NLuc-tdT, Fig. 5a). Lenti-S-NLuc-tdT enables sensitive detection of Spike-mediated viral entry over eight orders of magnitude by NLuc assay, and its fluorescent reporter allows viral detection in individual live cells by flow cytometry with minimal interference from cellular autofluorescence.

To test if SARS-CoV-2 Spike can mediate entry into human lung macrophages, we purified EPCAM^{-}CD31^{-}CD206^{+} macrophages from freshly resected human lung tissue. The primary lung macrophages survived in culture for up to a week with minimal decrease in viability. When the purified lung macrophages were exposed to lenti-S-NLuc-tdT at 1 TCID25 (titer at which 25% of HeLa-ACE2/TMPRSS2 were infected) and then cultured for 48 hours, infection was demonstrated by robust expression of luminescence (1-1.5×10^5 RLUs), whereas the control lentivirus lacking SARS-CoV-2 spike protein did not elicit measurable luminescence (Fig. 5b).

Treatment of the purified lung macrophages with hydroxychloroquine, a lysosomal protease inhibitor, or cytochalasin D, a potent inhibitor of phagocytosis previously shown to block macrophage entry of bacteria and virus[59,60], did not block infection by lenti-S-NLuc-tdT across a wide range of concentrations (10^{-2} – 10^2 uM) (Fig. 5c). This indicates that Spike-mediated entry into lung macrophages does not require phagocytosis. We next performed neutralization assays using three potent anti-Spike monoclonal antibodies (mAbs) at various stages of preclinical and clinical testing, including an ACE2-competing anti-RBD antibody (COVA2-15). Although each of these mAbs robustly inhibited lenti-S-NLuc-tdT infection of HeLa-ACE2/TMPRSS2 at nanomolar concentrations (Fig. 5d), none reduced lenti-S-NLuc-tdT infection of purified lung macrophages (Fig. 5e). Thus, Spike-mediated entry into lung macrophages occurs by a potentially novel mechanism that does not require phagocytosis or the ACE2-interacting receptor binding motif (RBM) of the SARS-CoV-2 Spike protein.

DISCUSSION

We established an experimental model of COVID-19 initiation in the human lung by productive infection of *ex vivo* cultured human lung slices with SARS-CoV-2. scRNA-seq and smFISH generated a comprehensive atlas of SARS-CoV-2 lung cell tropism and allowed us to probe the viral life cycle and its dynamic effects on the corresponding host gene expression program of individual lung cell types, by reconstruction of "infection pseudotime" from the single cell profiles of infected intermediates. The results indicate that the most susceptible lung target of SARS-CoV-2 and focus of inflammation is activated interstitial macrophages. In this newly characterized lung macrophage subtype, viral RNA amplification results in host cell takeover with viral transcripts comprising up to 60% of the total cellular transcriptome. During takeover, there is cell-autonomous induction of an interferon-dominated inflammatory response, including induction of five chemokines that can recruit local innate immune cells expressing the cognate receptors, including DCs (via *CCL2*, *CCL13, CXCL10*), neutrophils (*CCL8, CCl13*), and additional macrophages (*CCL8, CCL13*) forming an autocatalytic cycle, as well as CD4 and CD8 T cells (*CXCL10*). Takeover also induces expression of cytokine *IL6*, the potent inflammatory molecule central to cytokine storm[57], which can signal to many immune cells and most structural cells of the lung. Thus, SARS-CoV-2 infection and takeover of interstitial macrophages and interferon-dominated induction of this suite of chemokines and cytokines forms a focus of lung inflammation and immune infiltration, which we propose initiates the transition from COVID-19 pneumonia to ARDS as elaborated below.

Our scRNA-seq and smFISH analyses indicate that SARS-CoV-2 can also infect alveolar macrophages, as previously surmised[21,23]. However, in contrast to activated interstitial macrophages, there is neither viral takeover of the host cell transcriptome nor cell-autonomous

induction of a substantial inflammatory response. This could be due to effective host control or destruction of the virus in alveolar macrophages, or to viral evasion of detection[61] in order to complete its replication cycle (see accompanying manuscript). As other studies have also identified the importance of macrophage infection to COVID-19 pathogenesis[21-23], our results highlight the need in future COVID-19 studies to resolve the molecular subtype of lung macrophages infected, the extent of their viral takeover, and the specific host cell response, in evaluating the role of infected macrophages in the disease.

Our proposed cellular model of COVID-19 pathogenesis is shown in Fig. 6. Among the first cells encountered by virions reaching the alveoli are alveolar macrophages patrolling the airspace, which engulf the virions but show only a limited host cell response ("containment focus"). Virions that elude these macrophages infect alveolar epithelial cells, most notably alveolar type 2 cells[62], which express the SARS-CoV-2 receptor *ACE2* and protease *TMPRSS2*[42]. Virus propagation can lead to high viral RNA levels that presumably alter and destroy AT2 cells ("replication focus"), injuring the alveolar epithelium and compromising its repair and its barrier function, initiating viral pneumonia. Once virus encounters and infects interstitial macrophages, either through transepithelial spread or an epithelial breach, viral takeover of these macrophages triggers the inflammatory phase of COVID-19 by induction of a specific suite of cytokines and chemokines. These not only recruit and activate the local immune cells noted above, but signaling via IL6 to lung structural cells including alveolar capillary cells may damage and increase capillary permeability[63,64], causing fluid accumulation and clotting. This also amplifies the inflammatory response through recruitment of circulating immune cells into the airspace, resulting in the respiratory demise (hypoxemic respiratory failure) and pathology (diffuse alveolar damage) characteristic of COVID-19 ARDS [4,65]. Breakdown of the endothelial barrier

would also facilitate spread of the virus and release of IL6 and other lung inflammatory signals into the bloodstream, commencing the systemic effects of cytokine storm[57].

The central role in the model of infected interstitial macrophages in the transition of COVID-19 pneumonia to ARDS and cytokine storm implies that blocking their infection would prevent the most serious consequences of COVID-19. In this regard, our finding that therapeutically relevant mAbs do not neutralize SARS-CoV-2 Spike-mediated entry into purified lung macrophages, although they do block ACE2- and Fcγ-receptor-mediated entry into human blood monocytes[22] and bone-marrow derived macrophages in humanized mice[23], has important medical implications. It suggests that SARS-CoV-2 enters lung resident macrophages by a different mechanism than is targeted by current COVID-19 entry inhibitors, which have been largely developed and evaluated based on SARS-CoV-2 Spike binding affinity to ACE2, the canonical receptor for AT2 cells, or neutralization activity assayed in ACE2-expressing cell lines. This could explain why clinical mAbs do not work in severe COVID-19 – they block viral entry into airway and alveolar epithelial cells that initiate the disease, but not the macrophages we propose catalyze the inflammatory phase (Fig. 6e). The differential expression of several classes of SARS-CoV-2 host factors only in the activated IMs, including receptors (*CD209*, *NRP1*), proteases (*CTSL*) that support entry and proteolytic cleavage of SARS-CoV-2 Spike, and host factors that support viral replication (*KMT2C*) and virion assembly (*NPC1*) (Extended Data Fig.6) suggests a handful of high priority alternative entry pathways for mechanistic validation to block viral entry and takeover of activated IMs. Effective therapies to prevent the onset or reverse the progression of severe COVID-19 ARDS should address both the noncanonical pathways of viral entry and the molecular and cellular consequences of the downstream inflammatory cycles.

Our approach for elucidating the molecular and cellular basis of COVID-19 initiation relied on: productive infection of a human lung slice system and scRNA-seq pipeline that allowed culture, capture, and gene expression analysis of both viral and host transcriptomes in comprehensive cell types of the native organ; careful comparison with freshly-harvested tissue to distinguish direct virus-induced changes from culture-induced effects; and development of the computational method "infection pseudotime" to reveal the cell-intrinsic gene expression program induced by viral infection. Future improvements should focus on increasing the capture efficiency of viral subgenomic transcripts to resolve gene-level viral expression in single cells, and on development of whole mount preparations of human lung slices and a means to visualize gene expression, viral destruction of alveoli, and infiltrating immune cells in three-dimensions and in real time. Our approach can be used to elucidate the initiation program and evaluate therapeutics for any human lung infection at cellular resolution.

METHODS

Ex vivo culture of human lung tissue

Fresh, normal lung tissue was procured from organ donors that have exhausted therapeutic recipient options through Donor Network West, or intraoperatively from surgical resections at the Stanford Medical Center. Case 1 was a male organ donor aged 62. The entire lung was obtained en bloc, and the left upper lobe (LUL) was selected based on clear imaging as indicated on the donor report. Case 2 was a female organ donor aged 36 with a history of M to F gender reassignment. The entire left lung was obtained, and the LUL was selected based on clear imaging as indicated on the donor report. Case 3 was a 57-year-old-female with a history of fatty liver disease, diagnosed with stage two adenocarcinoma, who underwent left lower lobe (LLL) lobectomy. Case 4 was an 83-year-old female with a distant smoking history, diagnosed with stage two adenocarcinoma, who underwent LUL lobectomy. Case 5 was a male organ donor aged 57. The entire lung was obtained en bloc, and small sections were cut from RUL, RML, and RLL, based on clear imaging as indicated on the donor report. Case summaries are provided in Table S4.

In each case, proximal (airway) and distal (alveolar) regions were resected and cut into 300-500 µm slices with platinum coated double edge blade (Electron Microscopy Sciences 7200301) manually. Both airway and alveolar slices (3 or 4 total) were cultured in the same well in a 12-well plate with or without precoating of 500 µL of growth factor reduced Matrigel (Corning 354230), 1 mL DMEM/F12 media supplemented with GlutaMAX (Gibco 35050061) 10% fetal bovine serum (FBS, Gibco 10-082-147), 100 U/mL Penicillin-Streptomycin (Gibco 15140122), and 10 mM HEPES (N-2-hydroxyethylpiperazine-N-2-ethane sulfonic acid, Gibco 15630080), and incubated at 37ºC, 5% CO_2.

Tissue samples obtained from surgical resections were obtained under a protocol approved by the Stanford University Human Subjects Research Compliance Office (IRB 15166) and informed consent was obtained from each patient before surgery. All experiments followed applicable regulations and guidelines.

The research protocol for donor samples was approved by the DNW's internal ethics committee (Research project STAN-19-104) and the medical advisory board, as well as by the Institutional Review Board at Stanford University which determined that this project does not meet the definition of human subject research as defined in federal regulations 45 CFR 46.102 or 21 CFR 50.3.

Cell lines

VeroE6 cells were obtained from ATCC as mycoplasma-free stocks and maintained in supplemented DMEM (DMEM (Dulbecco's Modified Eagle Medium) (Thermo 11885-092) with 1X L-glut (Thermo SH30034), MEM nonessential amino acids (Thermo 11140050), 10mM HEPES (Gibco 15630-080), 1X antibiotic/antimycotic (Life Technologies SV30079), and 1mM sodium pyruvate (Gibco 11360-070)) with 10% heat-inactivated (HI) FBS (Sigma F0926). Vero/hSLAM cells were a kind gift from Dr. Chris Miller and Dr. Timothy Carroll (University of California, Davis) and were mycoplasma free (PlasmoTest, Invivogen). VeroE6/TMPRSS2 cells[66] were obtained from the Japanese Collection of Research Bioresources Cell Bank as mycoplasma-free stocks. Vero/hSLAM and VeroE6/TMPRSS2 were maintained in supplemented DMEM with 10% HI-FBS and 1 mg/mL G418 sulfate (Thermo Fisher 10-131-027). HeLa/ACE2/TMPRSS2 cells were a generous gift from Dr. Jesse Bloom at the Fred Hutchinson Cancer Research Center.

SARS-CoV-2 infections

SARS-CoV-2 (USA-WA1/2020) was obtained in March 2020 from BEI Resources and passaged in VeroE6 cells in supplemented DMEM with 2% HI-FBS. Viral stocks were cleared of cellular debris by centrifugation (1,000*g,* 10 min, 4°C), aliquoted, and stored at -80°C. Titer was determined by plaque assay (see below). The viral stock was verified by deep sequencing (~100,000X coverage per base) against the reference sequence (GenBank MN985325.1), and all tissue replicates were infected with passage 3 virus. A purified stock ("WA1 new") was also made by passaging in Vero/hSLAM cells, then clarifying by centrifugation (4,000*g*, 10 min, 4°C) followed by three buffer exchanges of phosphate-buffered saline (PBS) using Amicon Ultra-15 100 kDa Centrifugal Filter Units (Millipore Sigma). This viral stock was also verified by deep sequencing. Infections of lung slices were performed in supplemented DMEM with 2% FBS at a multiplicity of infection (MOI) of 1 (assuming all lung cells in the culture could be target cells) at 37°C. After 2 hours, free virions were removed by washing the tissue with PBS, after which the slices were cultured in DMEM/F12 with 10% FBS for 24 or 72 hrs. All procedures involving infectious SARS-CoV-2 were performed inside a class II biosafety cabinet (BSC) in the CDC-approved Biosafety Level 3 (BSL3) facility at Stanford University under approved biosafety protocols. All stocks generated and used were between 0.5 and 2 x 10^6 pfu/mL.

Plaque assay

VeroE6 or VeroE6/TMPRSS2 cells were plated at 4.5-5 x 10^5 cells/well in a standard 12-well tissue culture plate (Falcon) one day prior to infection. On the day of infection, cells were washed once with PBS. Infected human lung slice culture supernatants were added to the monolayer undiluted or diluted as indicated in supplemented DMEM containing 2% FBS. After 45 min of rocking inside an incubator at 37°C under 5% CO_2 to allow viral adsorption to the cells, plates were overlaid in the BSC with a fresh, pre-warmed (37°C) 1:1 mixture of 2X MEM

(Thermo 11935046) (supplemented with 0.4% bovine Serum Albumin (BSA, Sigma A9576), 2X L-glutamate, 20mM HEPES, 2X antibiotic/antimycotic (Life Technologies), and 0.24% sodium bicarbonate (Sigma S8761)) and 2.4% Avicel (FMC Biopolymer). Plates were then returned to the incubator for 72h (VeroE6) or 48h (VeroE6/TMPRSS2) prior to overlay removal, washing with PBS, fixation with 70% ethanol, and staining with 0.3% crystal violet (Sigma). For the timecourse (Extended Data Fig.1), lung slices were infected and washed. At 24h the supernatant was harvested, stored frozen, and replaced completely with fresh media. At 72h, the supernatant was harvested and stored frozen. The supernatants were then thawed, and plaque assays performed on the same plate as above.

Viral inactivation and remdesivir treatment

UV inactivation of virus was performed by delivering 1800 MJ of UV-C light (254 nm) to 250 uL of undiluted viral stock in a 24-well plate using a Stratalinker 1800 (Stratagene California, La Jolla, CA) inside a BSC in the BSL3. For heat inactivation, one aliquot of thawed undiluted viral stock was placed in a heat block at 60°C for 20 minutes inside a BSC in the BSL3. Inactivations were verified by plaque assay. For remdesivir (RDV) treatment, 10 mM stocks of RDV (Gilead) in DMSO were prepared and added to lung slices cultures at the time of infection to a final concentration of 10 μM. Slices were re-dosed after washing off the virus inoculum.

Single-cell mRNA sequencing

Lung cell isolation

All fresh (non-cultured and non-infected) tissue was processed at BSL2, and all cultured or infected tissue was processed in BSL3.

BSL2: Normal lung tissue was obtained as described for the slice cultures. All tissues were received and immediately placed in cold PBS and transported on ice directly to the research lab. Individual human lung samples were dissected, minced, and placed in digestion media (400 µg/mL Liberase DL (Sigma 5466202001) and 100 µg/mL elastase (Worthington LS006365) in RPMI (Gibco 72400120) in a gentleMACS c-tube (Miltenyi 130-096-334). Samples were partially dissociated by running 'm_lung_01_01' on a gentleMACS Dissociator (Miltenyi 130-093-235), incubated on a Nutator at 37 °C for 30 min, and then dispersed to a single cell suspension by running 'm_lung_02_01'. Processing buffer (5% FBS in 1XPBS) and DNase I (100 µg/mL, Worthington LS006344) were then added, and the samples rocked at 37 °C for 5 min. Samples were then placed at 4 °C for the remainder of the protocol. Cells were filtered through a 100-µm filter (Fisher 08-771-19), pelleted (300*g*, 5 min, 4 °C), and resuspended in ACK red blood cell lysis buffer (Gibco A1049201) for 3 min, after which the lysis buffer was inactivated by adding excess processing buffer. Cells were then filtered through a 70-µm strainer (Fisher 22363548), pelleted again (300*g*, 5 min, 4 °C), and resuspended in 2% FBS in PBS.

BSL3: After washing off virus and incubating for the indicated times, lung slices were washed with PBS and carefully transferred to 15 mL conical tubes (Falcon) containing 5 mL digestion buffer (DMEM/F12 with 400 µg/mL Liberase DL (Sigma), 50 µg/mL elastase, and 250U benzonase (EMD Millipore 706643)) and incubated with manual or automatic rocking at 37°C for 1 hour, followed by serum neutralization of Liberase and elastase activity with 10% FBS in cold DMEM/F12 media. For infection 1 only, the tissue was then dissociated by running m_lung_02 on a gentleMACS dissociator inside the BSC. The tissue was then mashed through a 100 µM filter with a syringe insert (Falcon), and the filter was washed with additional cold DMEM/F12 with 10% FBS to recover any remaining cells. The cellular suspension was spun at

4°C at 300 x *g* for 5 minutes, washed, and exposed to 1mL cold ACK lysis buffer (Sigma) for 1 minute on ice. The lysis buffer was neutralized by dilution with 5 mL cold DMEM/F12 with 10% FBS, after which the cells were pelleted and resuspended in DMEM/F12 with 10% FBS, and the cells were stained with Trypan blue (Sigma T8154), sealed out of the BSC, and counted manually. For all steps, cells were kept at 0-4°C using a cold block (Eppendorf Isotherm system).

10x mRNA capture, library construction, and sequencing

BSL2: Cells isolated from normal lung tissue were captured in droplet emulsions using a 10x Chromium Controller (10x Genomics). cDNA was recovered and libraries were prepared using 10x Genomics 3' or 10x Genomics 5' Single Cell V3.1 protocol (infections 1,2,4 and 5 were sequenced using 3' chemistry, while infection 3 used both 3' and 5' technology), as described[32]. Sequencing libraries were analyzed (Agilent TapeStation D4150, using regular and high sensitivity D5000 ScreenTape) and balanced, and sequenced on a NovaSeq 6000 (Illumina).

BSL3: The 10x Genomics Single Cell protocols were performed as before, with the following modifications for BSL3. The 10x Genomics, 3' or 5' Single Cell v3.1 master mix was prepared outside the BSC. Within the BSC, cells prepared as above were added to the master mix in PCR tubes (USA Scientific 1402-4708) in a 96-well cold block (Ergo 4ti-0396) and the 10x chip was loaded per manufacturer's instructions, sealed, and processed in a 10x Chromium Controller in the BSC. The resultant cell/bead emulsions were loaded into PCR tubes and transferred immediately to a pre-warmed (53°C) PCR machine for cDNA synthesis carried out at 53°C for 45 minutes, then 85°C for 5 minutes, then 60°C for 15 minutes (plaque assays showed that exposure of SARS-CoV-2-infected samples at 60°C for 20 minutes in this manner rendered the sample non-infectious). After cDNA synthesis, samples were transferred out of the BSL3 for cDNA recovery, amplification, and sequencing library preparation as above.

Sequencing read alignment

Sequencing reads from single cells isolated using 10x Chromium were demultiplexed and then aligned to a custom built Human GRCh38 (GENCODE v30) and SARS-CoV-2 WA1 (GenBank: MN985325.1) reference using Cell Ranger (version 5.0, 10x Genomics).

Iterative cell clustering and annotation

Expression profiles of cells from different subjects were clustered separately using Python software package Scanpy (v1.7.2). For host genes, normalization was performed as described[32];Unique molecular identifiers (UMIs) were normalized across cells, scaled per 10,000 using the "sc.pp.normalize_total" function, converted to log-scale using the "sc.pp.log1p" function, and highly variable genes were selected with the "sc.pp.highly_variable_genes" function with a dispersion cutoff of 0.5, and scaled to unit variance and zero mean (z-scores) with the "scanpy.pp.scale" function, clipping values exceeding standard deviation 10. Principal components were calculated for these selected genes with the "sc.tl.pca" function. Clusters of similar cells were detected using the Leiden method ("tl.leiden" function) for community detection including only biologically meaningful principle components, as described[32], to construct the shared nearest neighbor map ("sc.pp.neighbors") and an empirically set resolution, visualized by uniform manifold approximation and projection (UMAP; "tl.umap" function).

Cells were iteratively clustered as described[32], with the following modifications. After separating clusters by expression of tissue compartment markers, cultured cell types generally segregated from their non-cultured counterparts. When possible, we assigned cell types to the canonical cell types using the most sensitive and specific markers identified in the human lung cell atlas[1]. For culture-induced subtypes that showed substantial transcriptional change, a representative marker gene was prepended to their canonical identity (e.g., IRF1+ aCap). If the transcriptional change

caused the cell type to lose markers that define their canonical identity, we named them based on the general type that could be assigned, and prepended a representative marker gene (e.g., KLF6+ Endo). If most of the cluster-specific markers were ribosomal or mitochondrial genes, they were labeled as low quality (e.g., Stromal-LQ). If most of the expressed genes were viral and we could not distinguish which cell type the cluster belonged to due to downregulation of marker genes, they were designated "infected" (e.g., Infected-LQ). Cells from different subjects with the same annotation were merged into a single group for all downstream analyses. Cell types that were exclusively found to be culture induced were grouped as "culture induced" (e.g., Induced Fibroblast) for viral tropism analysis.

Some native subtypes characterized by subtle transcriptional differences could not be resolved by droplet-based 10x sequencing (e.g., proximal subtypes for basal or ciliary cells, molecular subtypes of bronchial vessel cells, mast/basophils), and several rare (neuroendocrine cells, ionocytes) or anatomically-restricted cell types (e.g. serous cells in submucosal glands) were absent from the profiled lung tissue.

Viral takeover analysis

For the UMIs that aligned to the SARS-CoV-2 viral genome, raw UMIs were either directly converted to log scale ("log10(Viral UMIs + 1)") or explicitly divided by total cellular UMIs but not log-converted ("Viral UMIs"). Viral takeover trends were visualized by non-parametric Local Regression (LOESS, R stats version 3.6.2).

Viral pseudotime analysis

For viral pseudotime analysis, computations were performed in R using the Seurat package (v3). Infected alveolar macrophages (AMs) and activated interstitial macrophages (a-IMs) from

infection 1 were grouped, and counts were normalized using the 'SCTransform' command. Principal component analysis was performed using the 'RunPCA' command with default parameters and visualized with 'DimHeatmap'. To identify the major axes of variation within the infected macrophage subtypes that best correlated with SARS-CoV-2 RNA levels, the principal components with significant contribution from SARS-CoV-2 counts (among the top 15 genes with highest loadings) were selected for further inspection. PC.1 was found to be associated with increasing viral RNA levels in both AMs and a-IMs, and PC.2, PC.3, and PC.4 were found to be associated with increasing viral RNA levels only in a-IMs. To isolate the genes that specifically associated with increasing SARS-CoV-2 viral RNA levels in AMs, PC.3 was subtracted from PC.1 (see Extended Data Fig.5).

Thus, infection pseudotime was defined respectively for AMs and a-IMs as progression along the following axes by taking the following linear combinations of principal components:

$$\text{Infection pseudotime}_{\text{aIM}} = \text{PC. } 2 + \text{PC. } 3 + \text{PC. } 4$$

$$\text{Infection pseudotime}_{\text{AM}} = \text{PC. } 1 - \text{PC. } 3$$

AMs and aIMs were assigned respective pseudotime values that were normalized between 0 and 1.

Subgenomic RNA analysis

To detect viral subgenomic RNA junctions, we ran SICILIAN[41], a statistical wrapper that takes alignment files from a spliced aligner and calls true positive RNA splice junctions by employing a statistical model. SICILIAN assigns an empirical p-value to each detected junction in a 10x dataset, quantifying the statistical confidence of each detected junction being a truly expressed RNA junction. We used STAR v.2.7.5a as the aligner and aligned fastq files from all infections

to our custom built Human GRCh38 (GENCODE v29) and SARS-CoV-2 WA1 (GenBank: MN985325.1) reference. STAR was run in two-pass mode, in which the first pass identifies novel splice junctions and the second pass aligns reads after rebuilding the genome index with the novel junctions and its parameters were tuned to avoid bias against non-GTAG junctions as previously shown[67].

Immunostaining and single molecule in situ hybridization

BSL2: Samples were fixed in either 10% neutral buffered formalin, dehydrated with ethanol and embedded in paraffin wax, as described[32].

BSL3: Slices not taken for digestion were washed with PBS and transferred to 15 mL conical tubes containing 10% neutral buffered formalin (Sigma) and held at 4°C for 72 hours prior to transfer out of the BSL3. Slices were then transferred to 15 mL conical tubes containing PBS prior to dehydration.

Sections (6 μm) from paraffin blocks were processed using standard pre-treatment conditions for each per the RNAscope multiplex fluorescent reagent kit version 2 (V2) Assay (Advanced Cell Diagnostics, (ACD)), or immunostaining RNAscope co-detection assay in which antibody labeling was carried out after RNAscope V2 assay, or RNAscope HiPlex Assay protocols. AlexaFluor plus secondary antibodies (488 plus, anti-mouse, Invitrogen A32723; 750, anti-rabbit, Invitrogen A21039) were used at 1:1,000. For RNAscope V2 assays, TSA-plus fluorescein, Cy3 and Cy5 fluorophores were used at 1:500 dilution. Micrographs were acquired with laser scanning confocal fluorescence microscopy (Leica Stellaris 8) and processed with ImageJ and Imaris (version 9.2.0, Oxford Instruments). smFISH experiments were performed on lung tissue from at least two human participants distinct from the donors used for sequencing, and quantifications were based on at least 10 fields of view in each. For smFISH, fields of view

were scored manually, calling a cell positive for each gene probed if its nucleus had at least three associated expression puncta.

The following primary antibodies were used at 1:100: CD68 (mouse, Abcam ab955), RAGE (rabbit, Abcam ab216329). The following V2 RNAscope probes were used: *MSR1* (ACD 468661), *RNASE1* (ACD 556551), *FABP4* (ACD 470641); the following HiPlex probes were used: *ACE2* (ACD 848151), *DPP4* (ACD 477549), *EPCAM* (ACD 310288), *COL1A2* (ACD 432721), *PTPRC* (ACD 601998), *ASPN* (ACD 404481), *nCoV2019-S* (ACD 848561), *nCoV2019-orf1ab-sense* (ACD 859151), *CLDN* (ACD 517141), *EDNRB* (ACD 528301), *AGER* (ACD 470121), *SFTPC* (ACD 452561), *CD4* (ACD 605601), *CD3-pool* (ACD 426621), *CD8A* (ACD 560391), *MARCO* (ACD 512231), *STAB1* (ACD 472161), *FABP4* (ACD 470641), *FOXP3* (ACD 418471), *IER3* (ACD 1000371).

Macrophage isolation and culture

Lung tissue was obtained as described above for the slice cultures. All tissues were received and immediately placed in cold PBS and transported on ice directly to the research lab. Individual human lung samples were dissected, minced, and placed in digestion media (400 µg/mL Liberase DL (Sigma 5466202001) and 100 µg/mL elastase (Worthington LS006365) in RPMI (Gibco 72400120) in a gentleMACS c-tube (Miltenyi 130-096-334). Samples were partially dissociated by running 'm_lung_01_01' on a gentleMACS Dissociator (Miltenyi 130-093-235), incubated at 37 °C for 30 min, and then dispersed to a single cell suspension by running 'm_lung_02_01'. Processing buffer (5% fetal bovine serum in PBS) and DNase I (100 µg/mL, Worthington LS006344) were then added, and the samples rocked at 37 °C for 5 min. Samples were then placed at 4 °C for the remainder of the protocol. Cells were filtered through a 100-µm filter (supplier), pelleted (300g, 5 min, 4 °C), and resuspended in ACK red blood cell lysis buffer

(Gibco A1049201) for 3 min, after which the buffer was inactivated by adding excess processing buffer. Cells were then filtered through a 70-µm strainer (Fisherbrand 22363548), pelleted again (300g, 5 min, 4 °C), and resuspended in magnetic activated cell sorting (MACS) buffer (0.5% BSA, 2 mM EDTA in PBS) with Human FcR Blocking Reagent (Miltenyi 130-059-901) to block non-specific binding of antibodies. The isolated lung cells were stained with MACS microbeads conjugated to EPCAM and CD31 (Miltenyi 130-061-101, 130-045-801) then passed through an LS MACS column (Miltenyi, 130-042-401) on a MidiMACS Separator magnet (Miltenyi, 130-042-302). The "EPCAM^{-}CD31^{-}" flowthrough was collected and stained with CD206 antibodies conjugated to biotin (Miltenyi 130-095-214), washed twice with MACS buffer, then stained with Anti-Biotin MicroBeads (Miltenyi 130-090-485) and passed through an LS MACS column on a MidiMACS Separator magnet, designated "EPCAM^{-}CD31^{-}CD206^{+}". The resulting population of purified macrophages were cultured in DMEM/F12 media supplemented with 10% FBS, 100 U/mL Penicillin-Streptomycin, and incubated at 37ºC, 5% CO2.

Pseudotyped lentivirus production

To create lenti-S-NLuc-tdT, Spike pseudotyped lentiviruses encoding a nanoluciferase-tdTomato reporter were produced in HEK-293T cells (5×10^6 cells per 10-cm culture dish) by co-transfection of a 5-plasmid system as described previously[58]. Based on the original lentiviral backbone plasmid (pHAGE-Luc2-IRES-ZsGreen, Addgene 164432), we replaced the Luc2-IRES-ZsGreen reporter with a cassette encoding H2B fused to Nanoluciferase (Promega) to minimize background luminescence, followed by a T2A self-cleaving peptide, and tdTomato fluorescent protein using gBlock synthesis (Integrated DNA Technologies). The 5-plasmid system includes a packaging vector (pHAGE-H2B-NanoLuc-T2A-tdTomato), a plasmid

encoding full-length Spike with a 21-residue deletion on the C-terminus (pHDM SARS-CoV-2-SpikeΔ21), and three helper plasmids (pHDM-Hgpm2, pHDM-Tat1b, and pRC-CMV_Rev1b). Transfection mixture was prepared by adding 5 plasmids (10 µg packaging vector, 3.4 µg Spike-encoding plasmid, and 2.2 µg of each helper plasmid) to 1 mL D10 medium (DMEM supplemented with 10% FBS, 1% Pen/Strep/L-Glutamine), followed by the addition of 30 µL BioT transfection reagent (Bioland Scientific, LLC, B01-03) in a dropwise manner with vigorous mixing. After 10-min incubation at room temperature, the transfection mixture was transferred to HEK-293T cells in the culture dish. Culture medium was replenished 24 hr post-transfection, and after another 48 hr, viruses were harvested and filtered through a 0.45-µm membrane. Spike-pseudotyped lentiviruses were aliquoted, stored at -80˚C, and titrated in HeLa/ACE2/TMPRSS2 cells before being used in neutralization assays.

Neutralizing antibodies

The variable heavy chain (HC) and variable light chain (LC) sequences for COVA2-15[68] (HC GenBank MT599861, LC GenBank MT599945) were codon optimized for mammalian expression. Fragments were PCR amplified and inserted into linearized CMV/R expression vectors containing the heavy chain or light chain Fc sequence from VRC01. COVA2-15 was expressed in Expi293F cells via transient transfection. CC6.35 and eCC6.33.3 were a gift from D. Burton[69,70].

Neutralization assay

Neutralization with monoclonal antibodies (mAbs) was validated on HeLa-ACE2/TMPRSS2 cells using Spike-pseudotyped lentiviruses with either a luciferase-ZsGreen or nanoluciferase-tdTomato reporter. Cells were seeded in white-walled, clear-bottom 96-well plates

(ThermoFisher Scientific, 165306) at a density of 8,000 cells per well 1-day before the assay (day 0). On day 1, mAbs were serially diluted in D10 medium and then mixed with lentivirus (diluted in D10 medium, supplemented with polybrene (Sigma-Aldrich, TR1003), 1:1000, *v/v*) for 1 hr before being transferred to HeLa-ACE2/TMPRSS2 cells. Culture medium was replenished 24 hr post-infection. On day 3, medium was removed and cells were rinsed with Dulbecco's Phosphate-Buffered Saline (DPBS, Gibco, 14190144) before 100 µL of luciferase or nanoluciferase substrates (BriteLite, Perkin Elmer, 6066769 or Nano-Glo, Promega, N1110, prepared per manufacturer's instructions) were added to each well. Luminescent signals were recorded on a BioTek Synergy™ HT or Tecan M200 microplate reader. Percent infection was normalized to cells only (0% infection) and virus only (100% infection) on each plate. Neutralization assays were performed in biological duplicates (macrophage purifications from distinct donors).

Neutralization with monoclonal antibodies (mAbs) in the human macrophage experiments was measured with Spike-pseudotyped lentiviruses with the nanoluciferase-tdTomato reporter. Macrophages were seeded in white-walled, clear-bottom 96-well plates (10,000-20,000 cells per well) 1-day before the assay (day 0). On day 1, mAbs were serially diluted in DMEM/F12 medium and then mixed with lentivirus (diluted in DMEM/F12 medium, supplemented with polybrene, 1:1000, *v/v*) for 1 hr before being transferred to macrophages. Culture medium was replenished 4 hr post-infection. On day 3, cells were rinsed with DPBS, and then luminescent signals were read out with the nanoluciferase substrate (Nano-Glo) as above.

Statistics and Reproducibility

All heat maps and plots with single cell expression data include every cell from indicated types, unless otherwise stated in the figure legend (numbers available in Supplementary Table 4). Dot

plots were generated using a modified version of Scanpy's 'pl.dotplot' (Fig. 2a, viral expression dot plot) with indicated expression cutoff, or a modified version of Seurat's 'DotPlot' function available on GitHub (in Figs. 3d, 4g, and Extended Data Fig. 6). Scatter plots for infection pseudotime were generated with ggplot2's 'geom_point' function, and trend lines were plotted with parameter 'method = "loess"' (Figs. 3g, 4da-f, Extended Data Fig. 5e) Violin plots were generated with Scanpy's 'pl.violin' function (Fig. 1c, left panel), or Seaborn's 'violinplot' and 'stripplot' functions (Fig. 2a) and show proportion of single cells at indicated expression levels. Bar plots were generated in Excel (Fig. 1c, right panel, 3f). Histogram plots were generated using Seaborn's 'histplot' function with log scale transformation on both x-axis and y-axis (Fig. 1d, lower panel). Cumulative distribution plot was generated using Seaborn's 'ecdfplot' function and plotted on a Matplotlib''logit' scale which implements the logistic distribution (in Fig. 1d, upper panel). Arcplots depicting number of subgenomic junctions was plotted using a custom Python function (available on Github). Differentially expressed genes along infection pseudotime were computed by taking the top 250 genes that contributed to each pseudotime trajectory (see Methods), and further tested using pseudotimeDE's 'runPseudotimeDE' function without subsampling testing against the asymptotic null distribution, with exact p-values indicated in Table S3. Differentially expressed genes between "Late" vs. "Early" macrophages along infection pseudotime were computed using Seurat's 'FindMarkers' function implemented using the default Wilcoxon Rank Sum test, with exact p-values indicated in Table S3. Immunostaining and smFISH experiments were performed on at least 2 human or mouse subjects distinct from the donors used for sequencing, and quantifications were based on at least 10 fields of view in each. For smFISH, fields of view were scored manually, calling a cell positive for each gene probed if its nucleus had at least three associated expression puncta. No

statistical methods were used to predetermine sample size. The experiments were not randomized and investigators were not blinded to allocation during experiments and outcome assessment.

Data Availability

Raw sequencing data, UMI tables, cellular annotation metadata, Seurat objects, and scanpy objects are being deposited and will be released as soon as possible (at latest, upon acceptance of this manuscript).

Code Availability

Code to reproduce the analyses and figures are being deposited and will be released as soon as possible (at latest, upon acceptance of this manuscript).

REFERENCES

1 CDC, N. C. H. S. *Leading Causes of Death, 1900-1998*, <https://www.cdc.gov/nchs/data/dvs/lead1900_98.pdf>

2 WHO. *Leading causes of death - Global summary estimates*, <https://cdn.who.int/media/docs/default-source/gho-documents/global-health-estimates/ghe2019_cod_global_2000_20194e572f53-509f-4578-b01e-6370c65d9fc5_3096f6a3-0f82-4c0c-94e2-623e802527c8.xlsx?sfvrsn=eaf8ca5_7>

3 Wang, C., Horby, P. W., Hayden, F. G. & Gao, G. F. A novel coronavirus outbreak of global health concern. *Lancet* **395**, 470-473, doi:10.1016/S0140-6736(20)30185-9 (2020).

4 Lamers, M. M. & Haagmans, B. L. SARS-CoV-2 pathogenesis. *Nat Rev Microbiol* **20**, 270-284, doi:10.1038/s41579-022-00713-0 (2022).

5 Bao, L. *et al.* The pathogenicity of SARS-CoV-2 in hACE2 transgenic mice. *Nature* **583**, 830-833, doi:10.1038/s41586-020-2312-y (2020).

6 Jiang, R. D. *et al.* Pathogenesis of SARS-CoV-2 in Transgenic Mice Expressing Human Angiotensin-Converting Enzyme 2. *Cell* **182**, 50-58 e58, doi:10.1016/j.cell.2020.05.027 (2020).

7 Winkler, E. S. *et al.* SARS-CoV-2 infection of human ACE2-transgenic mice causes severe lung inflammation and impaired function. *Nat Immunol* **21**, 1327-1335, doi:10.1038/s41590-020-0778-2 (2020).

8 Rockx, B. *et al.* Comparative pathogenesis of COVID-19, MERS, and SARS in a nonhuman primate model. *Science (New York, N.Y.)* **368**, 1012-1015, doi:10.1126/science.abb7314 (2020).

9 Munster, V. J. *et al.* Respiratory disease in rhesus macaques inoculated with SARS-CoV-2. *Nature* **585**, 268-272, doi:10.1038/s41586-020-2324-7 (2020).

10 Tian, S. *et al.* Pulmonary Pathology of Early-Phase 2019 Novel Coronavirus (COVID-19) Pneumonia in Two Patients With Lung Cancer. *J Thorac Oncol* **15**, 700-704, doi:10.1016/j.jtho.2020.02.010 (2020).

11 Zeng, Z. *et al.* Pulmonary pathology of early-phase COVID-19 pneumonia in a patient with a benign lung lesion. *Histopathology* **77**, 823-831, doi:10.1111/his.14138 (2020).

12 Varga, Z. *et al.* Endothelial cell infection and endotheliitis in COVID-19. *Lancet* **395**, 1417-1418, doi:10.1016/S0140-6736(20)30937-5 (2020).

13 Bradley, B. T. *et al.* Histopathology and ultrastructural findings of fatal COVID-19 infections in Washington State: a case series. *Lancet* **396**, 320-332, doi:10.1016/S0140-6736(20)31305-2 (2020).

14 Xu, Z. *et al.* Pathological findings of COVID-19 associated with acute respiratory distress syndrome. *Lancet Respir Med* **8**, 420-422, doi:10.1016/S2213-2600(20)30076-X (2020).

15 Liao, M. *et al.* Single-cell landscape of bronchoalveolar immune cells in patients with COVID-19. *Nat Med* **26**, 842-844, doi:10.1038/s41591-020-0901-9 (2020).

16 Wang, S. *et al.* A single-cell transcriptomic landscape of the lungs of patients with COVID-19. *Nat Cell Biol* **23**, 1314-1328, doi:10.1038/s41556-021-00796-6 (2021).

17 Rendeiro, A. F. *et al.* The spatial landscape of lung pathology during COVID-19 progression. *Nature* **593**, 564-569, doi:10.1038/s41586-021-03475-6 (2021).

18 Delorey, T. M. *et al.* COVID-19 tissue atlases reveal SARS-CoV-2 pathology and cellular targets. *Nature* **595**, 107-113, doi:10.1038/s41586-021-03570-8 (2021).

19 Melms, J. C. *et al.* A molecular single-cell lung atlas of lethal COVID-19. *Nature* **595**, 114-119, doi:10.1038/s41586-021-03569-1 (2021).

20 Horiuchi, S. *et al.* Immune memory from SARS-CoV-2 infection in hamsters provides variant-independent protection but still allows virus transmission. *Sci Immunol* **6**, eabm3131, doi:10.1126/sciimmunol.abm3131 (2021).

21 Grant, R. A. *et al.* Circuits between infected macrophages and T cells in SARS-CoV-2 pneumonia. *Nature* **590**, 635-641, doi:10.1038/s41586-020-03148-w (2021).

22 Junqueira, C. *et al.* FcgammaR-mediated SARS-CoV-2 infection of monocytes activates inflammation. *Nature*, doi:10.1038/s41586-022-04702-4 (2022).

23 Sefik, E. *et al.* Inflammasome activation in infected macrophages drives COVID-19 pathology. *Nature*, doi:10.1038/s41586-022-04802-1 (2022).

24 Salahudeen, A. A. *et al.* Progenitor identification and SARS-CoV-2 infection in human distal lung organoids. *Nature* **588**, 670-675, doi:10.1038/s41586-020-3014-1 (2020).

25 Youk, J. *et al.* Three-Dimensional Human Alveolar Stem Cell Culture Models Reveal Infection Response to SARS-CoV-2. *Cell Stem Cell* **27**, 905-919 e910, doi:10.1016/j.stem.2020.10.004 (2020).

26 Beumer, J. *et al.* A CRISPR/Cas9 genetically engineered organoid biobank reveals essential host factors for coronaviruses. *Nat Commun* **12**, 5498, doi:10.1038/s41467-021-25729-7 (2021).

27 Han, Y. *et al.* Identification of SARS-CoV-2 inhibitors using lung and colonic organoids. *Nature* **589**, 270-275, doi:10.1038/s41586-020-2901-9 (2021).

28 Hong, W. *et al.* A mouse model for SARS-CoV-2-induced acute respiratory distress syndrome. *Signal Transduct Target Ther* **6**, 1, doi:10.1038/s41392-020-00451-w (2021).

29 Sun, S. H. *et al.* A Mouse Model of SARS-CoV-2 Infection and Pathogenesis. *Cell Host Microbe* **28**, 124-133 e124, doi:10.1016/j.chom.2020.05.020 (2020).

30 Hassert, M. *et al.* mRNA induced expression of human angiotensin-converting enzyme 2 in mice for the study of the adaptive immune response to severe acute respiratory syndrome coronavirus 2. *PLoS Pathog* **16**, e1009163, doi:10.1371/journal.ppat.1009163 (2020).

31 Hoagland, D. A. *et al.* Leveraging the antiviral type I interferon system as a first line of defense against SARS-CoV-2 pathogenicity. *Immunity* **54**, 557-570 e555, doi:10.1016/j.immuni.2021.01.017 (2021).

32 Travaglini, K. J. *et al.* A molecular cell atlas of the human lung from single-cell RNA sequencing. *Nature* **587**, 619-625, doi:10.1038/s41586-020-2922-4 (2020).

33 Reyfman, P. A. *et al.* Single-Cell Transcriptomic Analysis of Human Lung Provides Insights into the Pathobiology of Pulmonary Fibrosis. *Am J Respir Crit Care Med* **199**, 1517-1536, doi:10.1164/rccm.201712-2410OC (2019).

34 Goldfarbmuren, K. C. *et al.* Dissecting the cellular specificity of smoking effects and reconstructing lineages in the human airway epithelium. *Nat Commun* **11**, 2485, doi:10.1038/s41467-020-16239-z (2020).

35 Habermann, A. C. *et al.* Single-cell RNA sequencing reveals profibrotic roles of distinct epithelial and mesenchymal lineages in pulmonary fibrosis. *Sci Adv* **6**, eaba1972, doi:10.1126/sciadv.aba1972 (2020).

36 Deprez, M. *et al.* A Single-Cell Atlas of the Human Healthy Airways. *Am J Respir Crit Care Med* **202**, 1636-1645, doi:10.1164/rccm.201911-2199OC (2020).

37 Vieira Braga, F. A. *et al.* A cellular census of human lungs identifies novel cell states in health and in asthma. *Nat Med* **25**, 1153-1163, doi:10.1038/s41591-019-0468-5 (2019).

38 Sikkema, L. *et al.* An integrated cell atlas of the human lung in health and disease. *bioRxiv*, 2022.2003.2010.483747, doi:10.1101/2022.03.10.483747 (2022).

39 Wilk, A. J. *et al.* A single-cell atlas of the peripheral immune response in patients with severe COVID-19. *Nat Med* **26**, 1070-1076, doi:10.1038/s41591-020-0944-y (2020).

40 Wilk, A. J. *et al.* Multi-omic profiling reveals widespread dysregulation of innate immunity and hematopoiesis in COVID-19. *The Journal of experimental medicine* **218**, doi:10.1084/jem.20210582 (2021).

41 Dehghannasiri, R., Olivieri, J. E., Damljanovic, A. & Salzman, J. Specific splice junction detection in single cells with SICILIAN. *Genome Biol* **22**, 219, doi:10.1186/s13059-021-02434-8 (2021).

42 Hoffmann, M. *et al.* SARS-CoV-2 Cell Entry Depends on ACE2 and TMPRSS2 and Is Blocked by a Clinically Proven Protease Inhibitor. *Cell* **181**, 271-280 e278, doi:10.1016/j.cell.2020.02.052 (2020).

43 Muus, C. *et al.* Single-cell meta-analysis of SARS-CoV-2 entry genes across tissues and demographics. *Nat Med* **27**, 546-559, doi:10.1038/s41591-020-01227-z (2021).

44 Jaitin, D. A. *et al.* Lipid-Associated Macrophages Control Metabolic Homeostasis in a Trem2-Dependent Manner. *Cell* **178**, 686-698 e614, doi:10.1016/j.cell.2019.05.054 (2019).

45 Lavin, Y. *et al.* Innate Immune Landscape in Early Lung Adenocarcinoma by Paired Single-Cell Analyses. *Cell* **169**, 750-765 e717, doi:10.1016/j.cell.2017.04.014 (2017).

46 Maynard, A. *et al.* Therapy-Induced Evolution of Human Lung Cancer Revealed by Single-Cell RNA Sequencing. *Cell* **182**, 1232-1251 e1222, doi:10.1016/j.cell.2020.07.017 (2020).

47 Adams, T. S. *et al.* Single-cell RNA-seq reveals ectopic and aberrant lung-resident cell populations in idiopathic pulmonary fibrosis. *Sci Adv* **6**, eaba1983, doi:10.1126/sciadv.aba1983 (2020).

48 Sahoo, D. *et al.* Transcriptional profiling of lung macrophages identifies a predictive signature for inflammatory lung disease in preterm infants. *Commun Biol* **3**, 259, doi:10.1038/s42003-020-0985-2 (2020).

49 Trapnell, C. *et al.* The dynamics and regulators of cell fate decisions are revealed by pseudotemporal ordering of single cells. *Nat Biotechnol* **32**, 381-386, doi:10.1038/nbt.2859 (2014).

50 Treutlein, B. *et al.* Reconstructing lineage hierarchies of the distal lung epithelium using single-cell RNA-seq. *Nature* **509**, 371-375, doi:10.1038/nature13173 (2014).

51 Song, D. & Li, J. J. PseudotimeDE: inference of differential gene expression along cell pseudotime with well-calibrated p-values from single-cell RNA sequencing data. *Genome Biol* **22**, 124, doi:10.1186/s13059-021-02341-y (2021).

52 Honda, K., Takaoka, A. & Taniguchi, T. Type I interferon [corrected] gene induction by the interferon regulatory factor family of transcription factors. *Immunity* **25**, 349-360, doi:10.1016/j.immuni.2006.08.009 (2006).

53 Diamond, M. S. & Farzan, M. The broad-spectrum antiviral functions of IFIT and IFITM proteins. *Nat Rev Immunol* **13**, 46-57, doi:10.1038/nri3344 (2013).

54 Verhelst, J., Hulpiau, P. & Saelens, X. Mx proteins: antiviral gatekeepers that restrain the uninvited. *Microbiol Mol Biol Rev* **77**, 551-566, doi:10.1128/MMBR.00024-13 (2013).

55 Rustagi, A. & Gale, M., Jr. Innate antiviral immune signaling, viral evasion and modulation by HIV-1. *J Mol Biol* **426**, 1161-1177, doi:10.1016/j.jmb.2013.12.003 (2014).

56 Schneider, W. M., Chevillotte, M. D. & Rice, C. M. Interferon-stimulated genes: a complex web of host defenses. *Annu Rev Immunol* **32**, 513-545, doi:10.1146/annurev-immunol-032713-120231 (2014).

57 Fajgenbaum, D. C. & June, C. H. Cytokine Storm. *The New England journal of medicine* **383**, 2255-2273, doi:10.1056/NEJMra2026131 (2020).

58 Crawford, K. H. D. *et al.* Protocol and Reagents for Pseudotyping Lentiviral Particles with SARS-CoV-2 Spike Protein for Neutralization Assays. *Viruses* **12**, doi:10.3390/v12050513 (2020).

59 Elliott, J. A. & Winn, W. C., Jr. Treatment of alveolar macrophages with cytochalasin D inhibits uptake and subsequent growth of Legionella pneumophila. *Infect Immun* **51**, 31-36, doi:10.1128/iai.51.1.31-36.1986 (1986).

60 Clement, C. *et al.* A novel role for phagocytosis-like uptake in herpes simplex virus entry. *J Cell Biol* **174**, 1009-1021, doi:10.1083/jcb.200509155 (2006).

61 Dalskov, L. *et al.* SARS-CoV-2 evades immune detection in alveolar macrophages. *EMBO Rep* **21**, e51252, doi:10.15252/embr.202051252 (2020).

62 Cagno, V. SARS-CoV-2 cellular tropism. *Lancet Microbe* **1**, e2-e3, doi:10.1016/S2666-5247(20)30008-2 (2020).

63 Maruo, N., Morita, I., Shirao, M. & Murota, S. IL-6 increases endothelial permeability in vitro. *Endocrinology* **131**, 710-714, doi:10.1210/endo.131.2.1639018 (1992).

64 Teuwen, L. A., Geldhof, V., Pasut, A. & Carmeliet, P. COVID-19: the vasculature unleashed. *Nat Rev Immunol* **20**, 389-391, doi:10.1038/s41577-020-0343-0 (2020).

65 Matheson, N. J. & Lehner, P. J. How does SARS-CoV-2 cause COVID-19? *Science (New York, N.Y.)* **369**, 510-511, doi:10.1126/science.abc6156 (2020).

66 Matsuyama, S. *et al.* Enhanced isolation of SARS-CoV-2 by TMPRSS2-expressing cells. *Proc Natl Acad Sci U S A* **117**, 7001-7003, doi:10.1073/pnas.2002589117 (2020).

67 Kim, D. *et al.* The Architecture of SARS-CoV-2 Transcriptome. *Cell* **181**, 914-921 e910, doi:10.1016/j.cell.2020.04.011 (2020).

68 Brouwer, P. J. M. *et al.* Potent neutralizing antibodies from COVID-19 patients define multiple targets of vulnerability. *Science (New York, N.Y.)* **369**, 643-650, doi:10.1126/science.abc5902 (2020).

69 Rogers, T. F. *et al.* Isolation of potent SARS-CoV-2 neutralizing antibodies and protection from disease in a small animal model. *Science (New York, N.Y.)* **369**, 956-963, doi:10.1126/science.abc7520 (2020).

70 Zhao, F. *et al.* Engineering SARS-CoV-2 neutralizing antibodies for increased potency and reduced viral escape. *bioRxiv*, 2022.2001.2006.475303, doi:10.1101/2022.01.06.475303 (2022).

71 Baggen, J., Vanstreels, E., Jansen, S. & Daelemans, D. Cellular host factors for SARS-CoV-2 infection. *Nat Microbiol* **6**, 1219-1232, doi:10.1038/s41564-021-00958-0 (2021).

Acknowledgements

We are grateful to the lung donors and Donor Network West for whole lung tissue, and to an anonymous financial donor for construction of a new BSL3 facility. We thank Amy Kistler (Chan-Zuckerberg Biohub) for viral stock sequencing assistance; Jaishree Garhyan, Geoffrey Ivison, and Michelle Leong (Stanford) for BSL3 support; Daphne Cooper (10x Genomics) for discussions on BSL3 implementation of 10x protocols; and Robert C. Jones (Stanford) for help in tissue and equipment procurement. We also thank members of the Blish and Krasnow labs for valuable discussions and comments on the manuscript, and Alexander Lozano for discussions on bioinformatic analyses. The SARS-Related Coronavirus 2, Isolate USA-WA1/2020, NR-52281 was deposited by the Centers for Disease Control and Prevention and obtained through BEI Resources, NIAID, NIH. Funding was provided by the Bill & Melinda Gates Foundation (C.A.B., M.A.K.), Chan Zuckerberg Biohub (C.A.B., S.R.Q.), the Burroughs Wellcome Fund Project 1016687 (C.A.B.), a Stanford Chem-H/Innovative Medicine Accelerator COVID-19 Response Award (C.A.B.), and the Howard Hughes Medical Institute (M.A.K.). Fellowship and training support was from National Institutes of Health (A.R., T32 AI007502 and K08 AI163369; G.M-C., T32 DK007217; A.W., T32 GM007364), American Cancer Society Postdoctoral Fellowship (S.K.J.), Stanford Graduate Fellowship and Stanford Cell and Molecular Biology Training Grant (T32GM007276) (Y.Z.), and Stanford Bio-X Interdisciplinary Graduate Fellowship (A.W.). C.A.B. is an investigator of the Chan Zuckerberg Biohub and M.A.K. is an investigator of the Howard Hughes Medical Institute.

Author Contributions

T.H.W., K.J.T, A.R., A.G., S.Q., C.K., C.A.B., and M.A.K. conceived the project and designed the lung slice culture, SARS-CoV-2 infection, lung cell isolation, scRNA-seq, and bioinformatic analysis strategy. T.H.W., W.T., J.S. and C.S.K. reviewed clinical or donor histories and coordinated patient care teams to obtain profiled tissues. J.B.S. and C.S.K. established and revised IRB protocol 15166 to optimize for single cell and lung slice culture preparations. A.R., G.M-C,, and C.A.B. built the BSL3 SARS-CoV-2 program at Stanford University. A.R., G.M.-C. and A.B. isolated, propagated, genotyped, titered, sequenced, and developed inactivation and inhibition methods for SARS-CoV-2 virions and fixation methods for infected tissues. A.R. performed lung slice culture infections, and plaque assays. T.H.W., K.J.T, A.R., Y.Z., S.K.J., A.G., G.M-C, A.B., A.J.W., and M.M. designed and processed tissue to single cell suspensions, and prepared sequencing libraries. T.H.W.,. and K.J.T processed and aligned sequencing data. T.H.W., K.J.T, A.R., Y.Z., S.K.J., and A.G. provided tissue expertise and annotated cell types. R.D. performed SARS-CoV-2 sequence alignment, implemented SICILIAN, and with T.H.W. and K.J.T. analyzed subgenomic junction results. T.H.W. and K.J.T implemented bioinformatic methods, including infection pseudotime. T.H.W., K.J.T and S.K.J. designed, performed, and analyzed multiplex in situ hybridization experiments. T.H.W., A.R., and D.X. designed, performed, and analyzed Spike-dependent macrophage entry experiments. J.B.S., S.R.Q., C.S.K., J.S., P.S.K., C.A.B. and M.A.K. supervised and supported the work. T.H.W., K.J.T, A.R., C.A.B., and M.A.K. interpreted the data and wrote the manuscript, and all authors reviewed and edited the manuscript.

FIGURE LEGENDS

Figure 1. Detection of virion production, viral RNA amplification, and subgenomic RNA in cultured human lung tissue infected ex vivo by SARS-CoV-2.

(a) Strategy for slicing, culturing, infecting, and analyzing human lung tissue from healthy, surgically resected or organ donor lungs. For donor lungs, the healthiest lobe was selected based on absence of inflammation or infection detected by qPCR or chest imaging in the donor summary. In each case, distal and proximal lung regions were sampled and manually sliced into 300-500 um sections with a platinum-coated blade. Slices were cultured (DMEM/F12 medium supplemented with 10% FBS and pen/strep) at 37ºC and subsequently exposed to SARS-CoV-2 virions for 2 hours, washed to remove free virions, and culturing continued for 24 or 72 hours to allow infection to proceed before assaying supernatant for virion production by plaque assay, preserving tissue in 10% NBF for histological staining and multiplex single molecule fluorescence hybridization (smFISH), or dissociating tissue for 10x single cell RNA sequencing (scRNA-seq). (b) Productive infection of lung slices from case 5 measured by plaque assay. Lung slices were mock-infected for 72 hours ("No virus") or infected with purified SARS-CoV-2/WA1 virions (estimated multiplicity of infection ~1, see Methods) without pretreatment of the virus ("Virus") or controls with virus pretreated with ultraviolet irradiation ("Virus+UV") or heat ("Virus +heat") to inactivate virus, or with the virus-infected culture treated with the viral RdRp inhibitor remdesivir (concentration, "Virus+RDV"). The supernatant was then harvested and plaque assay performed by adding the indicated dilution of supernatant to a monolayer of VeroE6 cells for 45 minutes at 37ºC, overlaying the culture with 2.4% Avicel cellulose, then continuing the culture for 72h prior to crystal violet staining to visualize the plaques formed by immobilized zones of cell lysis. (c) scRNA-seq analysis of cultured lung slices from case 5

infected with virus and indicated control conditions as in (b). Violin plot (left) shows viral RNA expression levels (Total number of Unique Molecular Identifiers (UMIs) for detected viral RNAs) in single cells, and bar plot (right) shows number of viral subgenomic RNA junctions detected by SICILIAN[41]. Canonical, transcription-regulatory sequence (TRS) mediated junctions from the 5' leader (TRS-L) to the 5' end of open reading frames in the gene body (TRS-B); noncanonical, all other subgenomic junctions detected that pass SICILIAN statistical test. (d) Bar graph (bottom) showing dynamic range of viral RNA molecules expressed (Total number of viral UMIs/cell) in profiled single cells (Count) from scRNA-seq of infected lung slice cultures from all cases as in (a) but from lung slices cultured as indicated for 0, 24, or 72 hours following exposure to SARS-CoV-2. Dashed lines (in Cumulative distribution, top), expression levels for 99%, 99.9% and 99.99% of profiled cells.

Figure 2. A comprehensive map of SARS-CoV-2 cell tropism in the human lung.

(a) Violin plot of viral RNA expression level (log10-transformed viral UMIs) in the single cells of each of the molecular cell types detected by scRNA-seq of the lung slice infections from cases 1-4. Dot plot above shows pseudo-bulk viral RNA expression level for each cell type; dot size indicates the percentage of cells in each type with detected expression of viral RNA (thresholded at $\geq$20 viral UMI), and shading shows mean level of expression for the cells that passed detected expression threshold. Blue asterisk, cell types in which a proliferative subpopulation was detected but merged with the non-proliferating population in this plot (note these include basal, macrophage, and NK/T cells, none of which were previously found to include a proliferating subpopulation in the native lung); green text, additional cell types not detected or annotated in our native human lung cell atlas[32]; grey text, cell types only observed in cultured lung slices. (b) RNAscope multiplex single molecule fluorescence in situ hybridization (smFISH) of infected

lung slice cultures from case 2 showing close-ups (boxed, split channels at right) of canonical (alveolar epithelial type 2 (AT2)) and novel (myofibroblast (MyoF), CD4 T cell) lung cell targets of the virus, as well as an infected cell at a late stage of infection as indicated by high expression of positive strand viral RNA detected with S probe (red) and little or no expression of negative strand viral RNA (Neg, yellow) or the cell type markers examined. Probes were: positive strand viral RNA (viral S, red), negative strand viral RNA (Neg, antisense viral orf1ab, yellow), the canonical SARS-CoV-2 receptor *ACE2* (white), compartment markers for the epithelium (*EPCAM*, magenta), stroma (*COL1A1*, magenta), and cell type markers identifying alveolar epithelial type 2 (AT2) cells (*SFTPC*, green), myofibroblasts (MyoF; *ASPN*, green), CD4 T cells (*CD3*, magenta; *CD4*, green; *CD8*, cyan). (c) RNAscope smFISH of lung slice cultures as above detecting infected macrophage subtypes: viral S (red), negative strand RNA (antisense Orf1ab, yellow), the canonical SARS-CoV-2 receptor *ACE2* (white) and a receptor (*DPP4*) used by the related MERS coronavirus (white), general macrophage marker *MARCO* (magenta), and activated interstitial macrophage (a-IM) markers *STAB1* (cyan) and *IER3* (green). Close-ups of boxed regions (right) show alveolar macrophages (AMs, $MARCO^{+}STAB1^{-}IER3^{-}$) that express few S puncta and no negative puncta, and activated interstitial macrophages (a-IMs, $MARCO^{+}STAB1^{-}IER3^{+}$) in early infection ("early a-IM") expressing few S puncta and abundant negative puncta, and a-IMs in late infection ("late a-IM") with abundant S and negative puncta. (d) RNAscope smFISH detecting interaction between infected a-IM ($MARCO^{+}IER3^{+}$) expressing viral S and negative strand RNA (antisense Orf1ab), and two CD4 T cells ($CD3^{+}CD4^{+}$) expressing viral negative strand RNA but not viral S. Split panels at right show individual channels. Scale bars, 10 μm.

Figure 3. Identity, tissue localization, and viral takeover of molecularly distinct macrophage populations in the human lung.

(a) Uniform Manifold Approximation and Projection (UMAP) projection of molecularly distinct macrophage subpopulations in cultured human lung slices from cases 1 and 4 identified by computational clustering of their individual 10x scRNA-seq expression profiles (colored dots). Note three major molecular types: alveolar macrophages (AM) and newly designated (see panel e) interstitial macrophages (IM) and activated interstitial macrophages (a-IM), plus a minor cluster of proliferating macrophages (boxed) that using distinguishing markers shown in panel c could be subclassified as proliferative AMs (AM-p) or proliferative IMs (IM-p) (expanded box). (b) Schematic of alveoli, with epithelial barrier (green) comprised of AT1, AT2, and AT2-s cells, and endothelial barrier of underlying capillary comprised of aerocytes and general capillary cells. AMs reside in the airspace, while IMs and a-IMs reside in the interstitium (grey) bounded by the basal surfaces of epithelium and endothelium of neighboring alveoli. (c) Heatmap of expression of general macrophage marker genes (rows) in the individual macrophages from (a) (columns) of the indicated subtypes (for visualization, randomly downsampled to < 80 cells), and top differentially expressed genes that distinguish the subtypes. Note all clusters express general macrophage marker genes, but each has its own set of selectively expressed markers. (d) Dot plot showing fraction of expressing cells and mean expression (among expressing cells) of AM markers and IM activation markers in the macrophage subtypes from (a). Encoded proteins with related functions are indicated by color of the gene names. (e) Tissue localization of macrophage subtypes by RNAscope single molecule fluorescence in situ hybridization (smFISH) and immunostaining in control, non-cultured human lung from case 2. Markers shown: general macrophage antigen CD68 (green, protein), AT1 antigen RAGE (white, protein), AM marker

FABP4 (cyan, RNA), and IM marker RNASE1 (red, RNA). Scale bar, 30 μm. Note AMs localized to the apical side of AT1 cells that comprise alveolar epithelium (interpreted to be alveolar airspace), whereas IMs localized to the basal side of AT1 cells and are bounded by epithelium (interpreted to be the interstitial space). (f) Quantification of anatomical localization of AMs and IMs. Cells with substantial (>80%) colocalization with RAGE AT1 antigen were scored as interstitial, and those without substantial colocalization with RAGE AT1 antigen (<20% to account for AMs contacting the apical side of AT1 cells, as schematized in b) and any other cells were scored as alveolar. (g) Viral RNA takeover of the host transcriptome (Viral UMIs/ Total Cellular UMIs) graphed against viral expression (Total Viral UMIs) in single cells of AMs (blue dots) and a-IMs (red dots) from the infected human lung slices from case 1. Note that beginning at ~70 viral RNA molecules (UMIs) per cell, viral RNA begins to rapidly increase to thousands of viral molecules per cell and dominate ("takeover") the host cell transcriptome (25-60% total cellular UMIs) in a-IMs, whereas in AMs viral RNA never exceeded a few hundred UMI per cell and 1-2% of the host transcriptome, even at corresponding viral RNA cellular loads.

Figure 4. Differential induction of host response and inflammatory genes in activated interstitial and alveolar macrophages shown by infection pseudotime.

(a) Viral takeover (Viral UMIs/ Total Cellular UMIs) graphed against viral infection pseudotime for AMs (red) and a-IMs (blue) from the infected human lung slices from case 1; grey shading indicates 95% confidence interval. Pseudotime was separately computed for AMs and a-IMs by taking a linear combination of principal components that best correlated with monotonic increase in viral expression, then linearly rescaling between 0-1. “Early” cells in each infection pseudotime trajectory were defined by normalized pseudotime < 0.2, and “Late” cells were

defined by normalized pseudotime > 0.8. (b-f) Host gene expression profiles of AMs and a-IMs plotted along infection pseudotime, as in (a). A differential expression test was performed on the top 250 genes with the highest loadings for the infection pseudotime axis, and the selected genes presented (b-f) (visualized for the AMs and a-IMs in infected human lung slices from case 1) were among those that had statistically significant association with infection pseudotime as indicated. (b) Early interferon response genes that were significantly associated with a-IM pseudotime trajectory. (c) Late interferon stimulated genes (ISGs) that were significantly associated with a-IM pseudotime trajectory. (d) Chemokine ligands that were significantly associated with a-IM pseudotime trajectory. (e) Cytokines that were significantly associated with a-IM pseudotime trajectory. (f) ISGs that were significantly associated with AM pseudotime trajectory. (g) Dot plots (left) showing discretized expression of chemokine/cytokine ligands that were differentially expressed between early and late pseudotime a-IMs (*CXCL10*, *CCL2*, *CCL7*, *CCL8*, *CCL13*, *IL6*, *IL10*) and AMs (*CXCL16*), and their cognate receptors (right) in human lung cells (all infected conditions from cases 1-4); only cell types and chemokines with detected expression are shown. Lines connect ligands with cognate receptor. Red, virally induced in a-IMs; blue, differentially virally induced in AMs. (h) Summary schematic depicting the six cytokine and chemokine genes induced in a-IMs during viral takeover (dot sizes scaled to percentage expression and shaded with mean expression as in g), and the lung cell targets of the encoded inflammatory signals predicted from expression of the cognate receptor genes. Outbound arrows from a-IMs, cytokine signaling to lung cell targets or chemokine recruitment of immune cells toward a-IMs.

Figure 5. Spike-mediated entry into purified lung macrophages is not phagocytosis- or ACE2-dependent.

(a) Strategy for purification, culture, and infection of human lung macrophages with a SARS-CoV-2 pseudotyped lentivirus. (Left panel) Diagram of lenti-S-NLuc-tdT, a lentivirus pseudotyped to express SARS-CoV-2 Spike (S) protein on its surface and also engineered to express the reporter gene (boxed) encoding nuclear-targeted nanoluciferase (H2B-Nluc) and tdTomato fluorescent protein, separated by a self-cleaving T2A peptide. (Right panel) Experimental scheme. Human lung tissue obtained from surgical resections or organ donors were dissociated fresh, then labeled for magnetic activated cell sorting (MACS) using antibodies for the indicated surface markers (CD31, EPCAM, CD206; +, marker-positive; -, marker-negative). Lung macrophages ($CD31^{-}EPCAM^{-}CD206^{+}$) were cultured (37°C, DMEM/F12 medium with 10% FBS and pen/strep) and infected by lenti-S-NLuc-tdT. After 4 hours, free virions were washed off and infection continued for 48 hours before quantification of infection by expression level of a lenti-S-NLuc-tdT reporter gene. (b) Luminescence readout (RLU, relative light units) of NLuc reporter assays of purified lung macrophages that were left uninfected as control (Cells) or infected with lenti-NLuc-tdT (No spike lentivirus control), or lenti-S-NLuc-tdT (Spike D614G), or lenti-S-NLuc-tdT (Spike Delta+). Each pseudovirus was tested at two concentrations (diluted 1:1 or 1:2 with growth media). (c) Effect of phagocytosis inhibitor cytochalasin D or lysosome inhibitor hydroxychloroquine (HCQ) on lenti-S-NLuc-tdT infection of purified lung macrophages. Cells were pre-exposed for 2 hr to the indicated concentration of inhibitor before addition of lenti-S-NLuc-tdT for 4 hr before washing. NLuc luminescence values measured 48-hr after infection were normalized to control (non-neutralized) viral infections in each plate. (d,e) Neutralization of SARS-CoV-2 pseudovirus (lenti-S-NLuc-tdT) by the indicated monoclonal antibodies (mAbs) against SARS-CoV-2 receptor binding domain (RBD) in cultured HeLa-ACE2/TMPRSS2 control cells (c) or purified human lung macrophages (d). An anti-HIV

antibody (HIV-Ab) served as a negative control in c. To allow mAb binding, virions were pre-treated with the indicated concentration of mAb for 1 hr before addition of virions to the cells. Nluc luciferase values are presented as mean ± s.d from two independent experiments; values were normalized to control (non-neutralized) viral infections in each plate.

Figure 6. Model of initiation, transition, and pathogenesis of COVID-19 ARDS

(a-d) Model of COVID-19 initiation in the human lung and transition from viral pneumonia to lethal COVID-19 ARDS. (a) SARS-CoV-2 virion dissemination and arrival in the alveoli. Luminal alveolar macrophages (AM) encounter virions shed from the upper respiratory tract that enter the lung. AMs can express low to moderate numbers of viral RNA molecules but "contain" the viral RNA from taking over the total transcriptome and show only a very limited host cell inflammatory response to viral infection. (b) Replication and epithelial injury. SARS-CoV-2 virions enter AT2 cells through ACE2, its canonical receptor, and "replicate" to high viral RNA levels, producing infectious virions and initiating viral pneumonia. (c) a-IM takeover and inflammation signaling. SARS-CoV-2 virions spread to the interstitial space through either transepithelial release of virions by AT2 cells or injury of the epithelial barrier, and enter activated interstitial macrophages (a-IMs). Infected a-IMs can express very high levels of viral RNA that dominate ("take over") the host transcriptome. Viral takeover triggers induction of the chemokines and cytokines shown, forming a focus of inflammatory signaling. (d) Endothelial breach and immune infiltration. The a-IM inflammatory cytokine IL6 targets structural cells of the alveolus causing epithelial and endothelial breakdown, and the inflammatory cytokines recruit the indicated immune cells from the interstitium or bloodstream, which floods and infiltrates the alveolus causing COVID-19 ARDS. Local inflammatory molecules are amplified by circulating immune cells, and reciprocally can spread through the bloodstream to cause

systemic symptoms of cytokine storm. (e) Distinct foci of viral infection in the human lung. Containment focus: Competent immune cells (e.g., alveolar macrophages) are infected by SARS-CoV-2, express low to moderate levels of viral RNA, but "contain" viral takeover. Replication focus: susceptible cells that express the canonical cognate receptor to the Spike protein (e.g., AT2 cells that express ACE2) are infected by SARS-CoV-2, and support viral replication, packaging and release. Inflammation focus, viral takeover of sensitive inflammatory cells (e.g. a-IMs) induces specific cytokines and chemokines that amplify and propagate tissue inflammation and injury.

Extended Data Figure Legends

Extended Data Figure 1. Virion production of cultured human lung slices infected by SARS-CoV-2 increases over time.

Plaque assays on VeroE6/TMPRSS2 cells as in Fig. 1 of supernatant collected serially at 24 hr and 72 hr from the same lung slice culture. Media was completely replaced after the harvest of supernatant at 24 hr.

Extended Data Figure 2. Classes and abundance of canonical and novel subgenomic junctions detected in cultured human lung slices infected by SARS-CoV-2.

SARS-CoV-2 subgenomic RNA junctions were identified in scRNAseq analysis of infected lung slice cultures from lung slices infected in all cases as individual sequence reads that mapped discontinuously on the viral genome, as called by SICILIAN (SIngle Cell precIse spLice estImAtioN)[41] using generalized linear statistical modeling for precise unannotated splice junction quantification in single cells. (a) Diagram of full-length SARS-CoV-2 genomic RNA (29,903 nt) showing annotated ORF positions, the common 5' "leader" transcription-regulatory sequence (TRS-L, red fill) that connects in viral subgenomic RNAs to gene body TRS-B elements (not shown) adjacent to each of the canonically recognized ORFs (other colors), and the 5' and 3' untranslated regions (UTRs, open fill) of the viral genome. (b-d) Examples of inferred subgenomic RNA structures (left panel) based on the type of subgenomic junction detected, alongside arc plots (right panel) visualizing all novel junctions detected for that subgenomic junction type across all infection replicates. (b) "Canonical" subgenomic junctions connect the common 5' "leader" transcription-regulatory sequence (TRS-L) to gene body (TRS-B) adjacent to each of the canonically recognized ORFs. (c) Rare "L-internal" junctions connect TRS-L to cryptic gene body fusion sites. These could represent aberrant jumps during

discontinuous transcription. (d) "Internal" junctions occur between any two internal sites within the gene body. (e) The most abundant "3'UTR" junctions occur between any internal site within the gene body and the 3' UTR of the genome. These are likely overrepresented due to the predominant bias in sequence reads to the 3'-end in the scRNAseq technology employed (10x Genomics).

Extended Data Figure 3. Identity and abundance of canonical and novel lung cell types detected in human lung slice cultures by scRNA-seq.

Hierarchical tree showing human lung molecular cell types and their annotations in the indicated tissue compartments following iterative clustering of scRNA-seq profiles of cells from cases 1-4 in each compartment. Numbers below cell type name show total abundance of the cell type, and the stacked bar plot indicates proportions detected from each condition of freshly profiled uncultured (Uncultured), cultured and mock infected (Mock), or cultured and infected (Infected). Black, canonical cell types per our healthy reference human lung cell atlas[32] (bolded, detected in > 1 lung slice dataset). Cell types in which a proliferative subpopulation was detected is indicated (p) with the number of proliferative cells given in parenthesis. Cell types that were difficult to distinguish via 10x expression profiles without full-length transcriptome were merged. Abbreviations: Cil, ciliated; Cil-px, proximal ciliated; Bas, basal; Bas-px, proximal basal; Bas-d, differentiating basal; Gob, goblet; Ser, serous; Ion, ionocyte; NE, neuroendocrine; AT1, alveolar epithelial type 1; AT2, alveolar epithelial type 2; AT2-s, signaling alveolar epithelial type 2. Art, artery; aCap, capillary aerocyte; gCap, general capillary; Bro, bronchial vessel; Lym, lymphatic. ASM, airway smooth muscle; VSM, vascular smooth muscle; Peri, pericyte; MyoF, myofibroblast; FibM, fibromyocte; AdvF, adventitial fibroblast; AlvF, alveolar fibroblast; LipF, lipofibroblast; Meso, mesothelial. CD4 M/E, CD4 memory/effector T cells;

CD4 Na, CD4 naïve T cells; Treg, regulatory T cells; CD8 TRM, CD8 tissue resident memory T cells; NK, natural killer cell. MP, macrophage; pDC, plasmacytoid dendritic cell; mDC, myeloid dendritic cell; maDC, mature dendritic cell; Mono C, classical monocyte; Mono NC, nonclassical monocyte; Mono Int, intermediate monocyte; Neu, neutrophil; Mast Ba, mast/basophil; Mega, megakaryocyte.

Extended Data Figure 4. Localization and morphology of interstitial and alveolar macrophages in the lung.

Additional examples as in Fig. 3e of RNAscope single molecule fluorescence in situ hybridization (smFISH) and immunostaining of alveolar (AM) and interstitial (IM) macrophages in non-cultured human lung of case 2, detecting general macrophage antigen CD68 (green, protein), AT1 antigen RAGE (white, protein), AM marker FABP4 (cyan, RNA), and IM marker RNASE1 (red, RNA). Scale bar, 10 μm.

Extended Data Figure 5. Distinct viral pseudotime trajectories in interstitial and alveolar macrophages.

(a) Uniform Manifold Approximation and Projection (UMAP) projection of alveolar macrophages (AM) and activated interstitial macrophages (a-IM) in infected human lung slices from 10x scRNA-seq from infections 1 and 4, as in Fig. 3. (b) Normalized expression of SARS-CoV-2 RNA in each cell as shown by the heat map scale. (c) Normalized value of a-IM viral pseudotime value as shown in Fig. 4a. (d) Normalized value of AM viral pseudotime value as shown in Fig. 4a. (e) Total viral RNA expression (log10(Viral UMIs + 1)) graphed against viral infection pseudotime for AMs and a-IMs.

Extended Data Figure 6. Expression of receptors and other SARS-CoV-2 host factors in different lung macrophage subtypes.

Dot plot of scRNA-seq results of freshly profiled human lung slice cultures from cases 1 and 4, as in Fig. 3 showing for each indicated macrophage subtype (AM, alveolar macrophage; IM, interstitial macrophage; a-IM, activated interstitial macrophage) the fraction of expressing cells (% Expression) and mean expression value among expressing cells (ln(UP10K+1) of key proviral host factors in the SARS-CoV-2 replication cycle previously identified in CRISPR-based functional genetic screens[71]. Genes are grouped based on different steps of the viral life cycle (black font) and their normal cellular functions (colored font). Dots representing genes differentially up-regulated in a-IMs are outlined in red, and dots representing genes differentially up-regulated in AMs are outlined in blue (adjusted p-value < 0.05).

Supplemental Tables

Table S1. Summary of viral subgenomic junction discovery from single lung cells using SICILIAN

Table S2. Human lung cell cluster identities and their abundances in each dataset

Table S3. Differentially expressed genes along infection pseudotime trajectory for alveolar and interstitial macrophages

Table S4. Clinical summaries of donors or patients of surgical resection

Table S1. Summary of viral subgenomic junction discovery from single lung cells using SICILIAN

GeneA	JuncPosR1A	GeneB	JuncPosR1B	Junction_type	numReads
SARS-CoV-2_S	21761	SARS-CoV-2_S	21789	Internal	168
SARS-CoV-2_L	64	SARS-CoV-2_ORF8	28255	Canonical	120
SARS-CoV-2_N	29370	3'UTR	29797	3'UTR	82
SARS-CoV-2_ORF6	27270	3'UTR	29716	3'UTR	69
SARS-CoV-2_L	64	SARS-CoV-2_E	26468	Canonical	69
SARS-CoV-2_ORF6	27360	3'UTR	29795	3'UTR	57
unknown	9462	3'UTR	29706	3'UTR	54
SARS-CoV-2_ORF6	27264	SARS-CoV-2_ORF6	27291	Internal	47
3'UTR	29710	3'UTR	29793	3'UTR	45
3'UTR	29685	3'UTR	29804	3'UTR	44
SARS-CoV-2_ORF10	29633	SARS-CoV-2_ORF10	29669	Internal	42
SARS-CoV-2_S	25008	3'UTR	29702	3'UTR	40
SARS-CoV-2_N	28735	3'UTR	29783	3'UTR	33
3'UTR	29710	3'UTR	29791	3'UTR	32
3'UTR	29711	3'UTR	29777	3'UTR	31
SARS-CoV-2_N	29361	3'UTR	29801	3'UTR	28
SARS-CoV-2_ORF7b	27876	3'UTR	29737	3'UTR	28
SARS-CoV-2_L	66	SARS-CoV-2_ORF6	27385	Canonical	27
unknown	1383	SARS-CoV-2_N	29494	Internal	27
3'UTR	29698	3'UTR	29775	3'UTR	24
SARS-CoV-2_L	65	SARS-CoV-2_S	25381	Canonical	24
SARS-CoV-2_L	69	SARS-CoV-2_ORF5	27041	Canonical	24
unknown	3247	3'UTR	29703	3'UTR	23
unknown	4647	3'UTR	29782	3'UTR	22
unknown	4972	3'UTR	29716	3'UTR	22
SARS-CoV-2_ORF5	27190	SARS-CoV-2_ORF6	27222	Internal	22
SARS-CoV-2_N	28289	3'UTR	29801	3'UTR	20
unknown	6247	3'UTR	29767	3'UTR	20
3'UTR	29728	3'UTR	29760	3'UTR	19
unknown	11375	3'UTR	29771	3'UTR	18
unknown	15193	3'UTR	29709	3'UTR	18
unknown	18245	3'UTR	29801	3'UTR	18

... (Truncated, full table available in S1)

32 (out of 982) novel junctions that pass SICILIAN from all infection experiments are shown, ordered by number of reads supporting the junction. The 5' and 3' positions of the junctions are indicated, along with their classification as Canonical, L-novel, Internal, or 3' UTR (see main text and methods).

Table S2. Human lung cell cluster identities and their abundances in each dataset.

	Infection 1				Infection 2	
	Uncultured	Mock	WA1	Total	Uncultured	Mock
Epithelial						
Club	154	7	36	197	1	104
Cil	474	9	105	588	-	408
Bas	175	11	64	250	-	275
Bas-d	-	6	39	45	-	170
Bas-p	13	-	21	34	-	-
Gob	-	-	-	-	-	138
Muc	-	-	-	-	-	-
AT1	117	94	222	433	275	3,240
AT2	871	52	247	1,170	2	1,425
AT2-s	-	-	-	-	-	-
AT2-p	-	-	-	-	2	63
Epi-LQ	-	-	-	-	-	-
Total	1,804	179	734	2,717	280	5,823
Endothelial						
Art	686	77	179	942	126	1,369
Vein	732	-	-	732	365	1,070
aCap	491	139	162	792	223	978
IRF1+ aCap	-	-	-	-	-	345
gCap	3,974	230	490	4,694	782	1,001
SOCS3+ CDKN1A+ gCap	-	-	-	-	-	205
gCap-LQ	-	-	-	-	235	3
FABP4+ Cap	-	-	-	-	-	76
HSP+ Cap	-	-	-	-	-	490
ITGA1+ Cap	-	-	-	-	-	309
NXN+ Cap	-	-	-	-	-	277
SCL6A6+ Cap	-	-	-	-	-	153
TXNRD1+ Cap	-	-	-	-	-	440
Art	-	-	-	-	-	634

... (Truncated, full table available in S2)

Identities and abundances of each cell type called in each human lung slice infection dataset (10x scRNA-seq) are shown, tabulated by condition (Truncated).

Table S3. Differentially expressed genes along infection pseudotime trajectory for activated interstitial or alveolar macrophages

	Differential expression along pseudotime$_{aIM}$	Differential expression in Late v.s. Early a-IMs	
Gene		Average log2 fold change	Adjusted p-value
SARS-CoV-2	8.1149E-42	6.30303524	2.445E-10
CXCL10	9.0855E-07	3.98309725	1.1321E-16
ISG15	4.4518E-27	3.49696958	1.0583E-20
CCL8	1.3366E-43	3.4062398	2.3358E-24
CCL2	4.601E-70	3.34843994	2.7395E-11
IFIT1	4.4127E-24	3.3157429	4.5859E-29
IFIT3	1.3904E-13	3.03980101	7.248E-22
C1QA	5.8923E-19	2.8280586	6.4094E-09
C1QC	6.3543E-18	2.69629738	3.1943E-13
CTSL	2.9743E-39	2.66312288	4.9961E-09
IFIT2	3.4721E-11	2.66116916	4.7031E-28
MX1	4.7628E-16	2.62887962	2.8888E-19
RSAD2	2.0708E-19	2.53229946	2.0584E-29
IFITM3	2.5275E-25	2.50070002	2.261E-10
MX2	4.7699E-31	2.43091267	1.2926E-13
CD163	2.4695E-15	2.42739846	3.6776E-08
IFI6	9.5292E-17	2.37655011	1.7828E-17
IDH1	1.0812E-20	2.28592808	3.7297E-13
CTSB	9.8137E-24	2.27982332	2.1707E-09
GLUL	1.5351E-26	2.24935947	1.2399E-08
CTSZ	7.071E-15	2.1923914	1.7481E-07
HMOX1	8.5399E-43	2.17150669	8.7087E-08
CCL13	4.8899E-29	2.10064297	6.5774E-13
MT-CO1	1.1742E-15	2.06019013	2.4868E-06
CTSC	1.3091E-19	2.02974734	2.5518E-12
LY6E	9.4666E-16	2.00857916	3.1497E-11
PARP14	2.5852E-22	2.00576468	1.747E-10
LGMN	1.5793E-15	1.9422845	8.03E-23
MNDA	6.4829E-15	1.92639204	5.8826E-15
AC124319.1	2.5969E-20	1.80841223	3.7503E-06
MS4A6A	9.1458E-33	1.80647442	3.203E-27
IFI44L	3.4082E-14	1.78436328	1.7296E-21

… (Truncated, full table available in S3)

Genes that are differentially expressed continuously along pseudotime$_{aIM}$ trajectory, and differentially expressed in late vs. early activated interstitial macrophages (a-IMs).

	Differential expression along pseudotime$_{AM}$	Differential expression in Late v.s. Early AMs	
Gene		Average log2 fold change	Adjusted p-value
IFI27	2.9747E-126	3.529006095	4.25401E-10
FABP4	8.4312E-257	2.728531587	3.12028E-13
TGM2	5.13654E-93	2.164015611	2.28187E-12
AGRP	4.0027E-116	2.041222663	3.91521E-11
APOC1	1.6691E-286	1.94062241	7.29881E-17
CD52	7.9173E-237	1.900501051	2.49712E-18
HAMP	1.07333E-49	1.824361347	0.018269352
C1QB	4.1835E-109	1.667218061	3.88209E-19
FDX1	3.6325E-152	1.627190736	7.17703E-12
CXCL16	3.09027E-89	1.594248276	0.074820523
FABP5	4.5183E-105	1.525951999	1.33742E-11
LGALS3	1.69666E-85	1.520404888	1.09703E-12
RBP4	1.8209E-142	1.499842648	1.06745E-08
HLA-DRB1	2.8825E-164	1.497499659	2.69931E-15
CES1	3.8234E-182	1.363429082	1.40927E-07
HLA-DPA1	3.4424E-156	1.357964574	5.30886E-15
FTL	2.6568E-104	1.333383887	5.2066E-16
GCHFR	4.3001E-199	1.271573136	4.55452E-10
C1QC	4.23264E-82	1.269276562	6.14802E-13
HLA-DPB1	8.5054E-190	1.258662251	1.66347E-14

… (Truncated, full table available in S3)

Genes that are differentially expressed continuously along pseudotime$_{AM}$ trajectory, and differentially expressed in late vs. early activated interstitial macrophages (AMs).

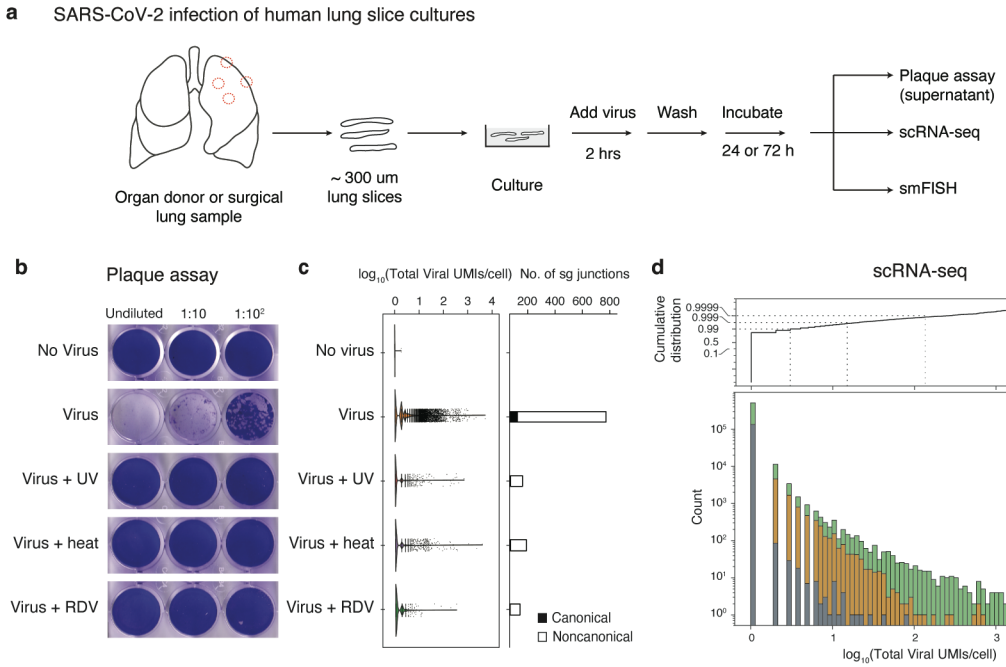

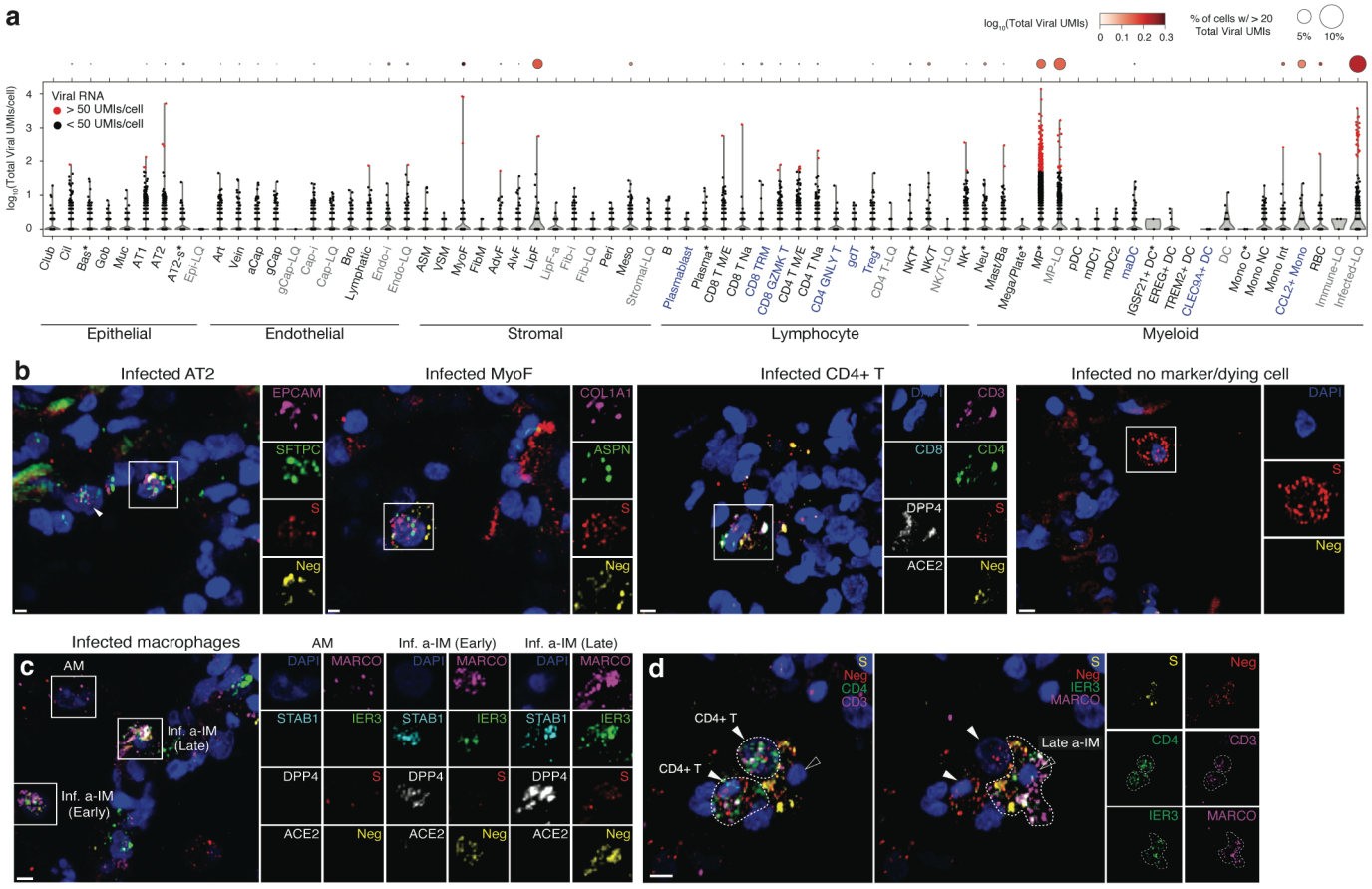

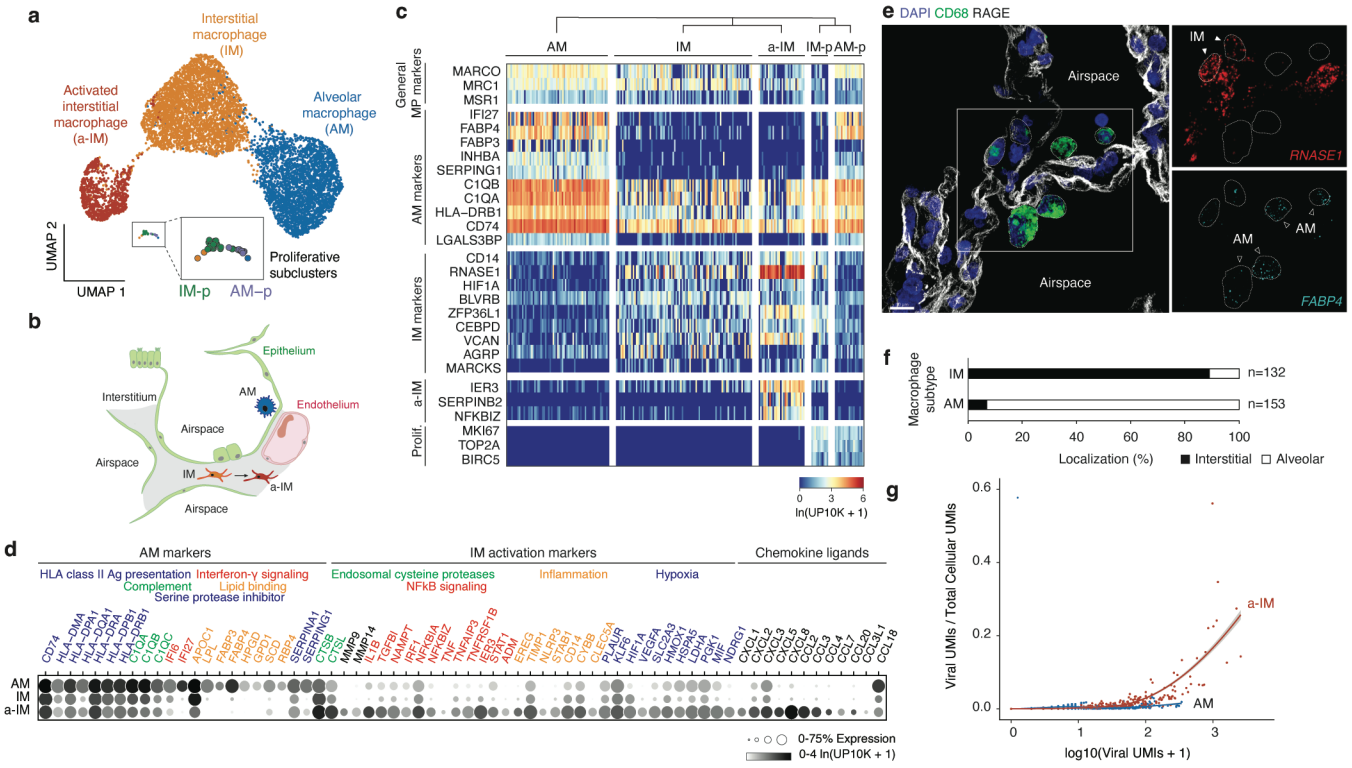

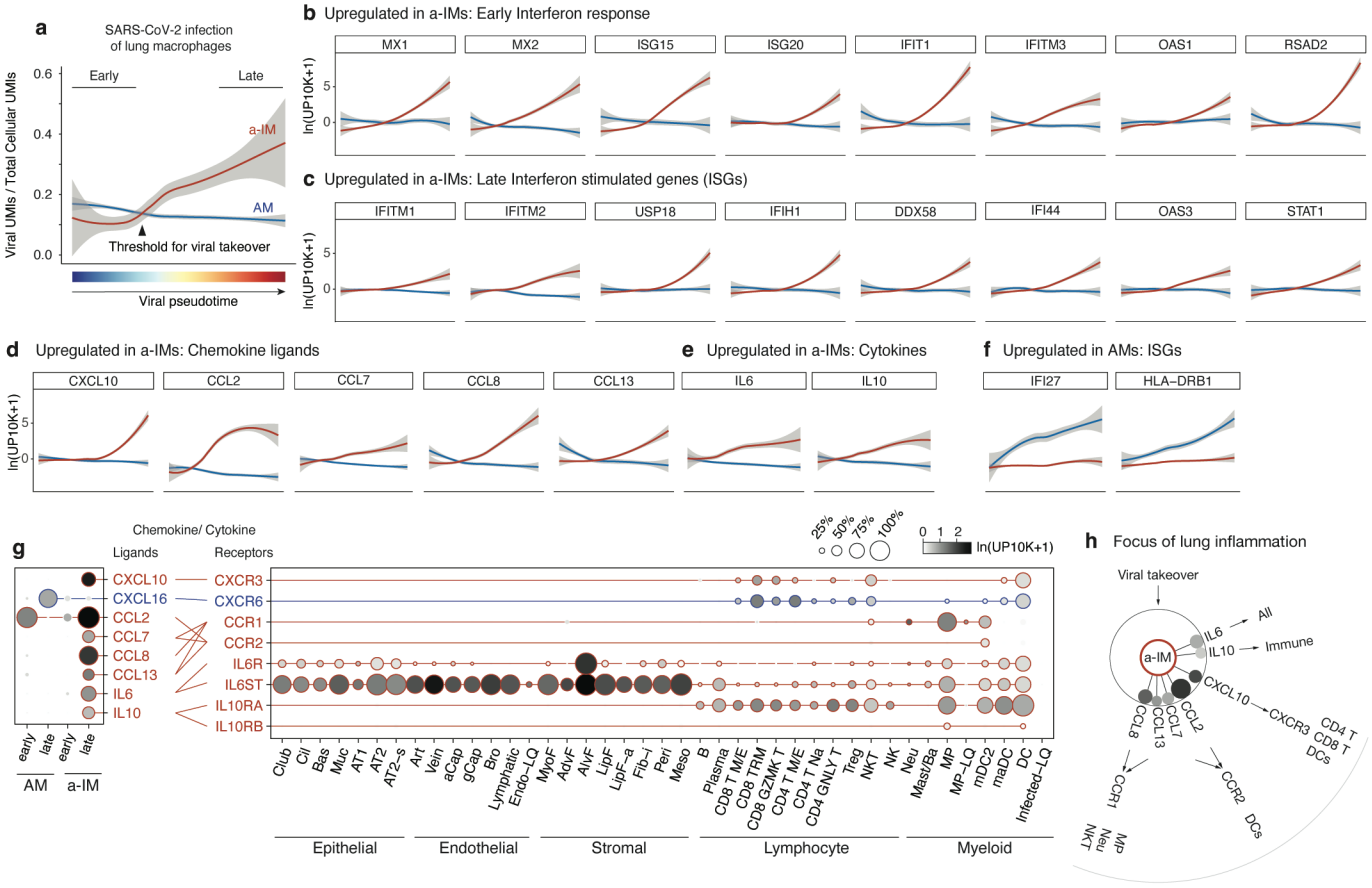

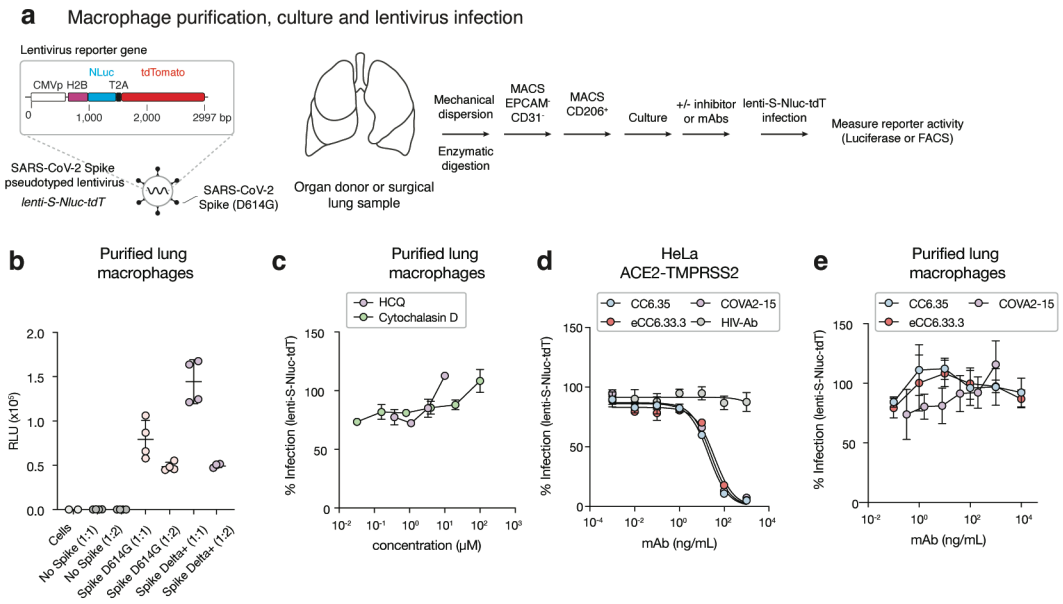

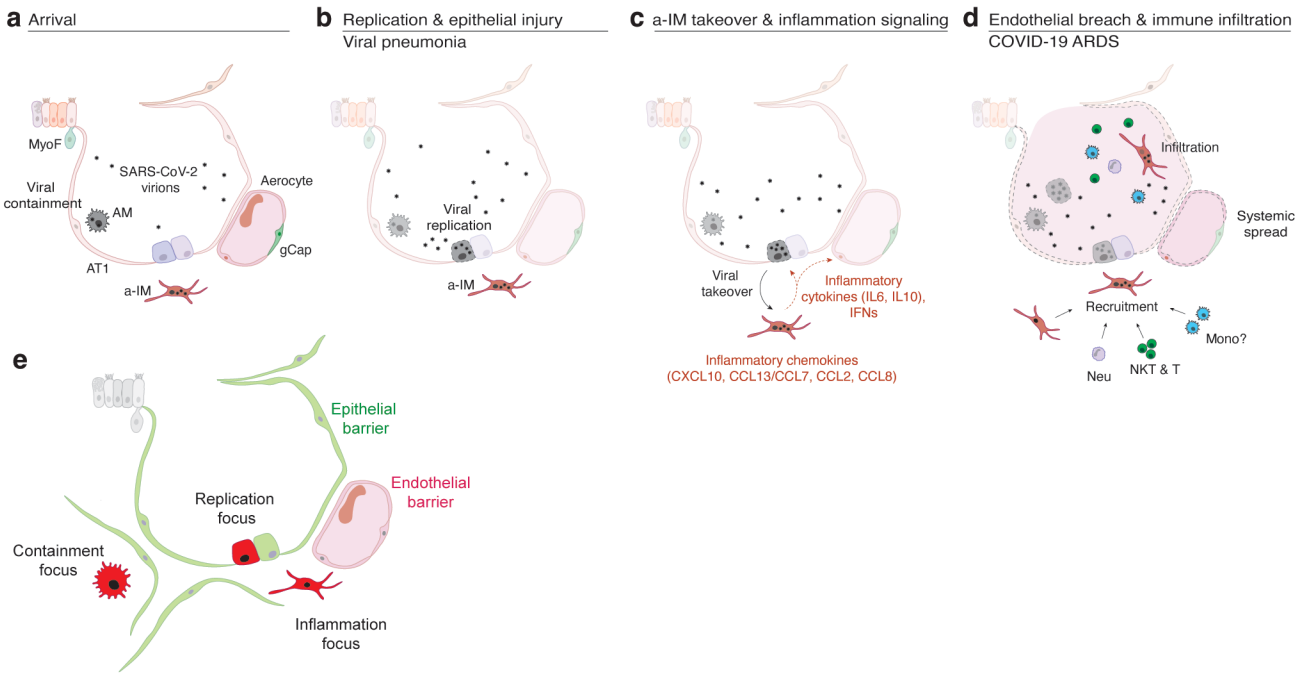

Extended Data Figure 1

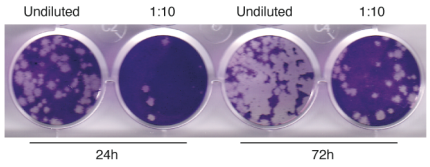

Extended Data Figure 2

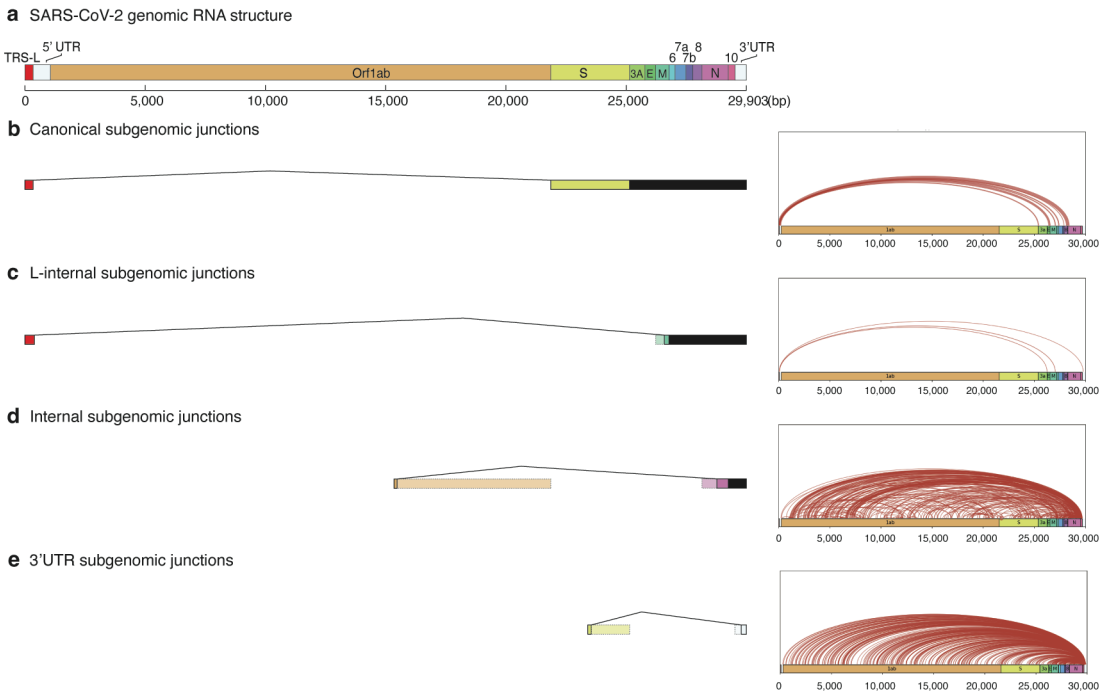

Extended Data Figure 3

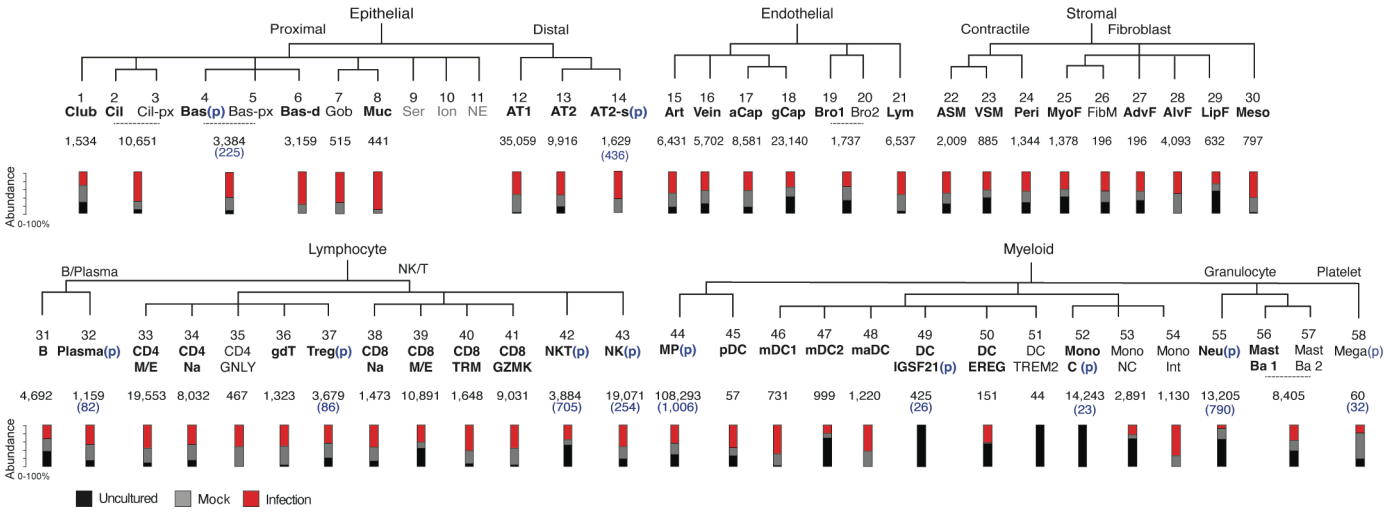

Extended Data Figure 4

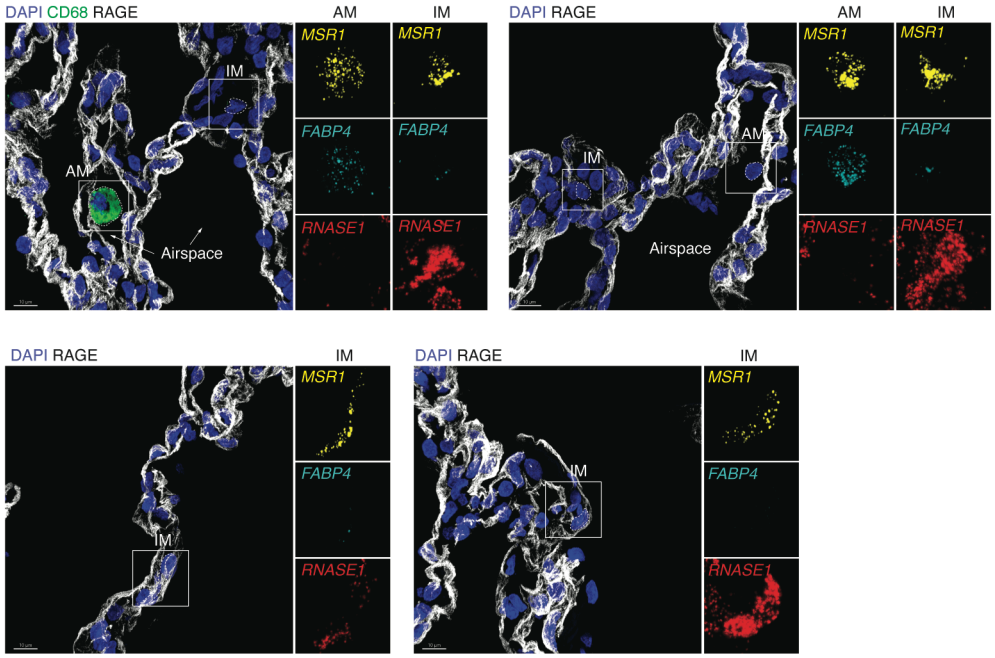

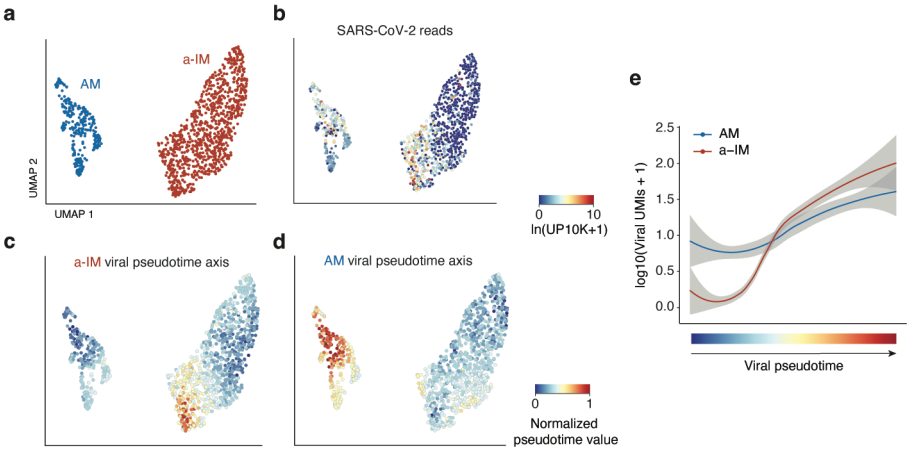

Extended Data Figure 6